

# Collaborative testing of eddy structure identification methods in free turbulent shear flows

J. P. Bonnet, J. Delville, M. N. Glauser, R. A. Antonia, D. K. Bisset, D. R. Cole, H. E. Fiedler, J. H. Garem, D. Hilberg, J. Jeong, N. K. R. Kevlahan, L. S. Ukeiley, E. Vincendeau

197

**Abstract** The thrust of this paper is to validate, test and compare several Coherent Structure eduction methods utilizing the same data base. The flow chosen was that of an experimental study of a plane, incompressible, fully developed turbulent two-stream mixing layer. The mixing layer was chosen as the data base because it has been studied extensively from a coherent structures point of view. In addition, its characteristics (similarity, convection velocities, etc.) are well

documented. There are also no wall effects so that comparisons between techniques are simplified. The data was collected from hot wire rakes with good spatial resolution thus allowing the contributors to apply and test different structure eduction techniques. The techniques chosen for discussion and used here have found wide utilization over the past decade, and all hold forth the promise of extensive application in the future. These include: Conditional Sampling (Vorticity-based and other methods); Wavelets; Pattern Recognition Analysis; Proper Orthogonal Decomposition; Stochastic Estimation; Topological Concept-based methods; Full Field Methods (e.g., pseudo flow visualization). All are illustrated by application to the mixing layer data base, and comparisons made between the results. This common study has shown that direct comparisons between results of several methods are now possible. Good quantitative and qualitative agreement between the different methods have been observed as well as some differences noted. As an example, the size of the averaged structures computed from the various methods compare to within 6 percent.

Received: 15 December 1994/Accepted: 18 December 1997

J. P. Bonnet, J. Delville, J. H. Garem, E. Vincendeau (§ 2, 4.2, 5, 8)  
C.E.A.T – Laboratoire d’Etudes Aérodynamiques UMR CNRS 6609,  
Université de Poitiers  
43 route de l’Aérodrome  
F-86036 Poitiers cedex, France

M. N. Glauser, D. R. Cole, L. S. Ukeiley (§ 4.2, 5)  
Department of Mechanical and Aeronautical Engineering  
Clarkson University  
Potsdam, NY 13699, USA

R. A. Antonia, D. K. Bisset (§ 7)  
Department of Mechanical Engineering  
University of Newcastle, N.S.W., 2308, Australia

H. E. Fiedler, D. Hilberg (§ 2.3, 4.3)  
Hermann-Föttinger-Institute  
Technical University of Berlin  
D-10623 Berlin, Germany

J. Jeong (§ 6)  
Dept. of Mechanical Engineering  
University of Houston, TX 77204-4792 USA

N. K. R. Kevlahan (§ 3)  
Department of Applied Mathematics and Theoretical Physics  
University of Cambridge  
Silver Street, Cambridge CB3 9EW, U.K.

Correspondence to: J. P. Bonnet or J. Delville

The results presented are part of a collaborative efforts that is being setup through the ERCOFTAC<sup>1</sup> Special Interest Group “Structure Identification Techniques for Free Turbulent Shear Flows”. Professor M. N. Glauser would like to acknowledge the National Science Foundation (Grant numbers CTS-9213607, INT-9016045 and MSM-8808872) for enabling the Clarkson effort.

<sup>1</sup>European Research Community On Flow Turbulence And Combustion.

## 1 Introduction

The existence and crucial role played by large-scale, organized motions in turbulent flows are now recognized by industrial, applied and fundamental researchers alike. It has become increasingly evident that coherent structures influence mixing, noise, vibrations, heat transfer, drag, etc. Two tasks which experimentalists or numerical analysts are faced with are: (1) how can these structures be separated from the background turbulence and (2) how can their averaged characteristics (in the more probable or dominant role sense) be determined? These tasks are non-trivial because the coherent structures are generally embedded in a random field and the technique used to determine when and where certain structures are passing or present is directly related to the definition of the coherent structures. Several methods for structure identification are available and the choice of a particular one can be dependent on the desired information. The choice depends not only on the definition of the structure, but also on the experimental and numerical capabilities available. For example, from an experimental point of view, some approaches require multiple sensors in order to obtain simultaneous instantaneous information at several spatial locations. Other approaches, however, only require knowledge at one or at most a few spatial locations. Moreover, it is necessary to choose the optimal experimental configuration in order to characterize the structures. The problem is equivalent to trying to find the simplest

(minimum) probe arrangement that gains maximum significant information about the structures. It is also related to the complexity of the organization of the flow and, in most cases, requires simultaneous three-dimensional measurements of the flow variables such as velocity. Certainly one can state, without question, that the recent rapid advances in, for example, data collection, flow simulation, instrumentation, digital data processing, and increased computational, graphical and storage capabilities of computers have resulted in an exponential increase in the application of various methods.

Recently, it has become clear that the different techniques available for the identification of eddy structures are in a mature enough state to justify comparisons between them. There is an obvious need for direct collaborative efforts to identify common features of the various techniques and to address some of the following questions:

- What is the state of the art of structure identification?
- How do these approaches work?
- What kind of information can be obtained from the various methods: instantaneous results, vorticity, averages, statistics, etc.?
- How do the results from different techniques compare with one another?
- What are the new directions in detection methods, and, correspondingly, what are their implications for turbulent flow analysis and prediction methods?

Results of collaborative effort<sup>2</sup> to address these issues are presented in this paper. The bulk of the results included here were obtained by the six participating laboratories before the Poitiers workshop. However, additional studies had to be performed to improve comparisons between results, the reliability of the results, and, to a lesser extent, to provide additional information. Hence, a post-workshop effort was necessary to bring the material into publishable form.

The thrust of this paper is to validate, test and compare several CS education methods utilizing the same data base. The flow chosen was that of an experimental study of a plane, incompressible, fully developed turbulent two-stream mixing layer. The mixing layer was chosen as the data base because it has been studied extensively from the coherent structures point of view. In addition, its characteristics (similarity, convection velocities, etc.) are well documented. There are also no wall effects so that comparisons between techniques are simplified. The data was collected from hot wire rakes with good spatial resolution thus allowing the contributors to apply and test several different structure education techniques. It is necessary to have the rakes of probes with sufficient resolution if the purpose of the experiment is not simply to facilitate taking large quantities of single point data, but rather to understand the flow's large scale spatial and temporal structure.

A variety of detection or analysis methods (both multi and single-point) are now available or are in various stages

of development. The following list gives the main methods discussed here: Conditional Sampling (Vorticity-based and other methods); Wavelets; Pattern Recognition Analysis; Proper Orthogonal Decomposition; Stochastic Estimation; Topological Concept-based methods; Full Field Methods (e.g., pseudo flow visualization). Detailed descriptions of these methods can be found in several reference papers (see for example Adrian 1975; Antonia 1981; Glauser and George 1992; Lesieur 1993; Berkooz et al. 1993; Hussain 1993; Kevlahan et al. 1993; Udine 1994) to appreciate the need for these techniques one must understand the character of high Reynolds number, often turbulent, motions. As modern full Navier-Stokes computer simulations have made clear, knowing the data at many points in the flow does little in and of itself to make clear what is happening because of the chaotic nature of the flow. The key to understanding usually lies in what is done to the data to bring the underlying structure to the foreground. The techniques chosen for discussion and use here have found wide utilization over the past decade, and all hold forth the promise of extensive application in the future. All will be illustrated by application to the mixing layer data base, and comparisons will be made between the results.

It is now well known that two main types of flow organization exist in mixing layers, a quasi-2D spanwise aligned vortex tube with streamwise aligned vortices superimposed on them. It has been proposed (Pierrehumbert and Windall 1982) that the same flow phenomena govern the turbulent mixing layer as its laminar counter part (i.e., pairing, amalgamation, tearing, etc...). The visualizations of Brown and Roshko (1974) are widely recognized as being the first to identify the large scale spanwise vortex structure in the plane mixing layer, while Konrad (1976) and Breidenthal (1980) seem to have shown the first strong evidence of the streamwise aligned vortices. Several theories based on instabilities, such as Kelvin Helmholtz, have been developed to explain the formation and evolution of the primary (spanwise) and secondary (streamwise) vortical structures and are described in reviews by Ho and Huerre (1984) and Liu (1989). It appears now that, at the current level of understanding of the turbulent mixing layer, it is necessary to study the dynamics of the streamwise structures and their interactions with the better understood spanwise structures.

Bernal and Roshko (1986) conducted a visualization study to examine the streamwise aligned vorticity. In particular they studied their origin, interaction with the spanwise vorticity and their role in the development of the mixing layer. These authors described the streamwise streaks as warped vortex lines connecting two adjacent spanwise vortices. They found that the streamwise structures originated from a Reynolds number dependent instability of the spanwise vortices. The mean spacing of the streamwise structures was found to be 0.67 when normalized by the local mean spacing of the spanwise vortices and was also found to be independent of velocity ratio. Bernal and Roshko postulated that the streamwise vorticity plays a large role in the mixing process because it entrains unmixed fluid into the cores of the spanwise vortex tubes. It was also shown that the smaller scale secondary structures embedded in the spanwise rollers did not destroy the "coherence" of the spanwise rollers. They concluded that, although the three-dimensionality of the structure plays an important

<sup>2</sup>The results presented here were initiated at a workshop held on October 15 and 16, 1992 in Poitiers under the ERCOFTAC label (European Research Community On Flow, Turbulence and Combustion).

role in the development of the mixing layer, the dynamics of the large scale vortices are *by and large two-dimensional*.

The spanwise structure in the two-dimensional mixing layer was examined by Browand and Troutt (1980). They used a rake of 12 hot-wires across the span of the wind tunnel. Computer visualizations of the instantaneous hot-wire outputs showed that the large scale structures extended across the wind tunnel and that there was some spanwise irregularity. They inferred from this that the spanwise irregularity is related to interactions between adjacent vortices. Browand (1986) sums up some of the findings from several flow visualization experiments. One of the conclusions presented was the need for theoretical models. He proposed that the large scale motions behave as a dynamical system with relatively few degrees of freedom. He further speculated that the turbulent mixing layer exhibits chaotic behavior in both space and time. This appears to be the first suggestion that a dynamical system model may prove fruitful in the turbulent mixing layer.

Lasheras et al. (1986, 1988) and Lasheras and Meiburg (1990) experimentally studied the initial conditions which trigger the instabilities that generate the streamwise aligned structures. The shear layer examined was generated by a flat plate with a small amplitude sinusoidal perturbation in the spanwise direction. Lasheras et al. (1986) determined that streamwise vortex tubes were formed from the stretching of weak perturbed vorticity in the braids of the Kàrmàn vortices (i.e. the two-dimensional spanwise vortical structures). The formation of these vortex tubes was determined to be uncoupled with the formation of the spanwise tubes, yet further downstream they coupled through convective instabilities to form "an array of spanwise vortices tangled with the counter-rotating pairs of axial vortices." In Meiburg and Lasheras (1988), it was found that the redistribution, reorientation and stretching of the spanwise vorticity led to counter-rotating pairs of three-dimensional streamwise vortex tubes consistent with Lasheras's earlier work. Strong streamwise vorticity was found to form only in the downstream half of the braids due to the free stagnation points forming close to the "downstream roller".

Bell and Mehta (1992) conducted an experimental study to establish "quantitatively" the presence and role of the secondary vortical structures in the mixing layer. They postulated that the streamwise structure originated from streamwise vortices in the upstream boundary layer. They found the circulation of the streamwise vortices to be 10% of that of the spanwise vortices. Also, they found that the vortices initially appeared in groups of three, then unwrapped to form a row of alternating-sign streamwise vortices consistent with the findings of Meiburg and Lasheras (1988). They showed evidence of the streamwise vortices in the self-similar region although their strength was decaying. It was concluded that one of the major effects of the streamwise vortices was to produce higher Reynolds stress values.

Moser and Rogers (1993) studied a temporally evolving simulated turbulent mixing layer for evidence of coherent structures. They found that there is a fundamental difference between the coherent structures found in the self-similar (asymptotic) region and those found in the transitional region or the laminar counterpart. They observed that in this region there were neither pairings nor rib vortices. Their results

showed that the turbulence in the braid region is qualitatively the same as that in the roller. These results strongly disagree with the findings of the flow visualization results. They proposed a possible explanation that the experiments have stronger two-dimensional disturbances than those that would arise from the receptivity of the splitter plate tip. Their findings show that a model for the mixing should not be based on the quasi two-dimensional structure, as has been done in the past, since their only dynamical significance appears to be that they create a strain and rotation-dominated region and do not influence the growth rate of the mixing layer.

All of these studies clearly show that the mixing layer provides a rich environment for the examination of coherent structures. Moreover, they also indicate that much work is still necessary to further our understanding of their role in this flow. It is evident that the various structure identification techniques utilized need to lead to an understanding of the dynamics of the structures. This step is particularly important if the ideas of coherent structures are to be implemented for prediction and control.

A brief overview of the techniques implemented for this collaborative study follows. The goal here is to articulate in an integrated fashion what each technique requires for application. In addition we wish to explain what can be gleaned from their application to further our understanding of coherent structures and their use for prediction and control. Descriptions of the individual techniques are included in their respective sections. Some of the techniques discussed require vectorial information from multiple sensors; whereas others may only require scalar (single velocity component for example) information at one or, at most, a few positions.

The Pseudo Flow Visualization (PFV) techniques, developed for quick and simple visual analysis of raw data from hot-wire rakes, utilizes the instantaneous signal from all sensors. Essentially, instantaneous velocity profiles at each time step are plotted. Following the evolution of these profiles in time gives a sense of the structure in the flow.

Various conditional methods utilize a range of the information given. These methods allow one to determine the average structure (most dominant in some sense as dictated by the particular approach). The Houston group describes an approach based on the Vorticity-Based Conditional Technique. A simpler version of this approach has been applied by the Newcastle group to detect small scale structures with intense spanwise vorticity. The dominant large scale structures are detected with the Window Average Gradient or WAG method (Bisset et al. 1990). The Delocalized Condition Sampling (Poitiers group) takes advantage of the multi-point data to perform structure detection. This method allows the user to automatically decide optimum detector placement, a distinct advantage over single-point conditional techniques.

It is not obvious how to integrate most of these methods into dynamical models for prediction and control. Perhaps one exception is the vorticity-based education scheme used by the Houston Group. It may be possible through a conditionally averaged equation, derived from the Navier-Stokes equations, to address the dynamics of physically occurring structures in the flow although to date such an approach has not been implemented. However, this concept can be directly related to the results obtained from LES (Ha Minh 1994).

Data from a minimum of two points is necessary for various applications of POD and LSE in turbulent flows. The POD has the advantage that a basis set is provided from which equations for the dynamics of coherent structures can be derived (see Aubry et al. 1988). Such a POD based low-dimensional dynamical systems approach for the mixing layer studied here is presently under development jointly by the CEAT/LEA in Poitiers (see Delville 1995) and by Clarkson University (see Ukeiley 1995). Information from all the probes is typically required if the phase (time dependence) of the POD structures is desired. However, as demonstrated in this paper, by using LSE in combination with POD (i.e., the Complementary Technique), the phase is obtainable with only two-point information. The Complementary Technique is possible since LSE successfully uses the conditional information specified about the flow (here the instantaneous velocity vector) at a few locations in conjunction with the two-point velocity correlations in order to estimate the instantaneous velocities throughout the entire flow. The Complementary Technique also provides a novel way for verification of POD based low-dimensional models.

The Wavelet Transform as introduced by Grossman and Morlet (1984) provides a mathematical tool which is capable of providing simultaneously both a wave-number and a physical space analysis. This is of particular importance when dealing with homogeneous and/or stationary directions in flows. Traditional Fourier analysis leads to basis functions (the dilated sine waves) which are perfectly localized in wave-number space but delocalized in physical space, a result which is not consistent with our concept of coherent structures (see Tennekes and Lumley 1972). The wavelet transform, on the other hand, preserve some degree of localization in both physical and wave-number space. The wavelet transform was applied by the Cambridge group to single-point time series from the multi-point data base. An interesting extension of this would be to apply the wavelet transformation to several of the cross-stream probes and examine the inhomogeneity from a wavelet point of view. Recent work of Higuchi et al. (1994) shows the utility of the wavelet transform for studying the dynamics of structures although the dependence of the results on the selection of the particular wavelet basis needs careful study.

Although not directly used here, Pattern Recognition Techniques (see Mumford 1982; Ferré et al. 1993) have been used as part of some structure identification schemes. The vorticity-based method and the conditional POD method use the Pattern Recognition concept to guide the selection of events. In addition, a topological analysis (see Perry and Chong 1986) has been applied to the data base by the Berlin group.

The remaining part of the paper is organized as follows. We first provide a description of the data base and its characterization by standard methods. The different approaches for structure eduction and/or analysis are then presented, and the corresponding results are given and discussed in their respective sections. A final section is devoted to a critical and comparative examination of the results and performances of the various techniques. Some prospective suggestions are then made based on these comparisons.

## 2

### Description of the data bases and global characterization

A brief description of the flow and of the measurement procedure is presented. Selected single point statistics are provided. The Pseudo Flow Visualization technique, topological analysis and conventional spectra are used to give some sense of the structural character of the data base.

#### 2.1

##### Experimental configuration

##### 2.1.1

###### Measurement apparatus and experimental procedure

The measurements are performed using multi-probe hot wires. Specially designed rakes of hot-wires have been built at the C.E.A.T. by Delville et al. (1989). These rakes can be aligned either in the inhomogeneous direction ( $Y$ ) or in the spanwise direction ( $Z$ ). The hot wires (W-Pt) are 0.5 mm long and 2.5  $\mu\text{m}$  in diameter. T.S.I. 1750 anemometers with bandwidths greater than 50 kHz are used. The probes are home-made subminiature probes, with a control volume of  $1 \times 1 \text{ mm}^2$ , and are embedded in a probe holder built from a printed circuit board. The resulting rakes have a frontal area of 1.6 mm in thickness, which minimizes their perturbations of the flow. The signals are simultaneously sampled at a maximum rate of  $f_s = 100 \text{ kHz}$  per channel with synchronized 12 bit A/D converters (one ADC per channel). An analog separation between mean and fluctuating voltages is performed to minimize quantization. The adjustment of the gains and the low-pass filtering frequency  $f_f$  of the signals is performed automatically under control of a micro-computer. Details on the probes and associated electronics are given in Bellin (1991) and Delville et al. (1993). Hot wire calibration is performed in a separate jet facility. The wire rake calibration takes into account temperature drift. An extended King's law:  $e(t)^2 = (T_w - T_f) (a + bv(t)^n)$  was used (Bruun 1995), where  $e(t)$  is the anemometer output voltage,  $T_w$  is the constant temperature of the wire and  $v(t)$  is the instantaneous velocity. The coefficients  $a$ ,  $b$ ,  $n$  as well as  $T_w$  were determined by a regression procedure. For the calibration of the rake of X-wires, 9 yaw angles  $\alpha$  were used over the range of  $-30^\circ$  to  $30^\circ$ . In this case, the coefficients  $a$  and  $b$  become dependent on  $\alpha(t)$  so that an iterative procedure is used for each time step.

##### 2.1.2

###### Flow configuration

The data are obtained from experiments performed in the fully developed region of a two-dimensional subsonic plane mixing layer with no streamwise pressure gradient. The two stream with velocities of  $U_a = 42.2 \text{ m s}^{-1}$  and  $U_b = 25.2 \text{ m s}^{-1}$  merge at the trailing edge of a splitter plate with a velocity ratio  $r = U_a/U_b = 0.59$ . An open loop wind tunnel is used. The velocity difference between the flows  $\Delta U = U_a - U_b$  is created by head-loss devices located upstream of the separating plate. The turbulence level in the external parts of the mixing layer is less than 0.3%. The two boundary layers at the trailing edge have conventional thicknesses ( $\delta_{99}$ ) of 9.6 and 6.3 mm and are fully turbulent. The test section is square ( $300 \times 300 \text{ mm}^2$ ) and

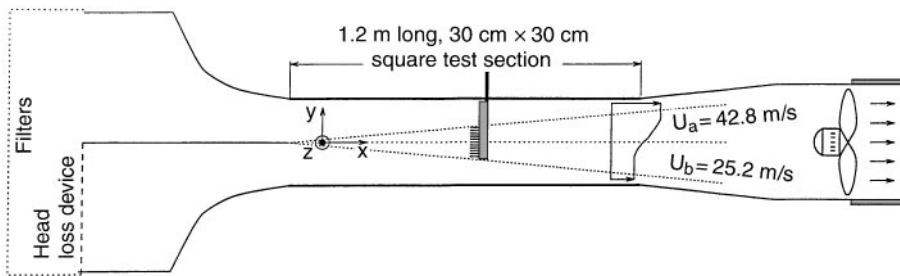


Fig. 1. Experimental configuration for the mixing layer experiment

1200 mm long. The reference frame in Fig. 1 is defined as follows:  $y$ , the direction normal to the plate ( $y=0$  on the mixing layer axis and  $y<0$  in the low velocity side);  $Z$ , the direction parallel to the trailing edge of the plate. The corresponding velocity components are  $u$ ,  $v$  and  $w$ , respectively.  $\delta_w$  is the vorticity thickness.

The self-similar region for the mean values begins at  $x = 300$  mm. Previous studies (Delville et al. 1987; Bellin 1991) have shown that the mixing layer behaves as expected from the literature, i.e., spreading rate  $\sigma = 43.15$ . Here the spreading rate is introduced by considering the mean longitudinal velocity profiles, in the self similar region:

$$\bar{u}(x, y) = U_b + (U_a - U_b)(1 - 0.5 \operatorname{erf}(\sigma y/x))$$

In Fig. 2a, the mean longitudinal velocity profiles, measured at 10 longitudinal locations, are presented normalized. This value of  $\sigma$  can be compared to the one corresponding to the step flow:

$$\sigma = \sigma_0 \frac{1+r}{1-r}$$

For the present velocity rate  $\sigma_0$  is found to be 11.33, very close to 11, the value given by Liepmann and Laufer (1947) for example. The integral scales  $\theta$  (momentum thickness) and  $\delta_w$  (vorticity thickness), measured in the self similar region, are plotted on Fig. 2b. The linear growth of the mixing layer is evident. The ratio  $\delta_w/\theta$  is around 4.88 and close to the value of 5 found by Browand and Ho (1983). Turbulent longitudinal, normal and shear stress profiles measured at  $X = 600$  mm from the trailing edge of the plate (where most testing has been performed) are shown plotted in Fig. 3. In this plot, the quantities measured by a single X-wire are compared with those obtained by using the hot-wire rake.

### 2.1.3

#### Data set

The measurements are performed in the self-similar region of the mixing layer. The data-base is collected from a rake of  $N_p = 12$  X-wire probes aligned in the  $Y$  direction at a downstream position of  $x = 600$  mm. A characteristic scale, about the size of the large quasi two-dimensional vortices in the plane mixing layer, can be defined from the inflectional mean velocity profile  $\bar{u}(y)$  by the velocity thickness  $\delta_w$ . In this case, the rake extent is of the order of  $2\delta_w$ , where  $\delta_w$  is the vorticity thickness:

$$\delta_w = \Delta U \left/ \left( \frac{\partial \bar{u}}{\partial y} \right)_{y=0} \right. \quad \text{and} \quad \Delta U = U_a - U_b$$

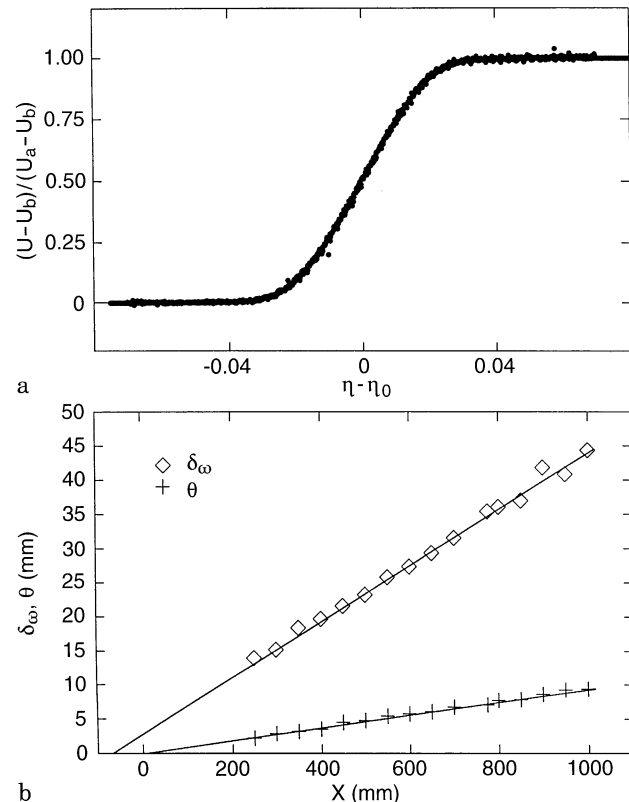


Fig. 2. a Normalised mean longitudinal velocity profiles measured at 10 longitudinal locations in the self preserving region of the mixing layer ( $300 \text{ mm} < X < 1000 \text{ mm}$  from the trailing edge of the plate); b Downstream evolution of momentum thickness  $\theta$  and vorticity thickness  $\delta_w$

The vorticity thickness is of the order of 30 mm (five times the probes separation  $\Delta Y$ ). Probes 1, 2 and 3 are located in the external low velocity part; and probes 10, 11 and 12 are in the high velocity external part. Probes 4 to 9 are located in the mixing zone of the flow.

Table 1 summarizes the main characteristics of the experiments.

Two sampling frequencies were used,  $f_s = 10$  kHz or 100 kHz, with corresponding low pass filtering frequencies of  $f_f = 5$  and 20 kHz, respectively. The time record lengths of the data are 819 200 time steps (more than 80 s) for the low sampling frequency and 10 240 time steps for the high sampling frequency (about 0.1 s). These time record lengths correspond to about 290 000 and 36 integral time scales, respectively.

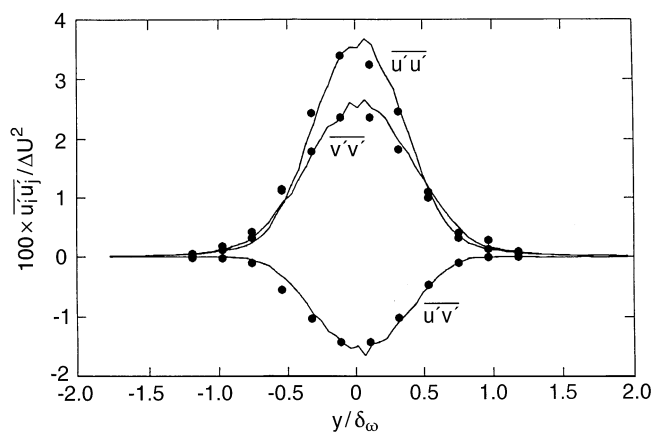


Fig. 3. Turbulent Reynolds stress measured at  $X=600$  mm from the trailing edge.  $\overline{u^2}$ ,  $\overline{v^2}$  and  $\overline{u'v'}$ . —Single X wire measurement ● rake measurement

In order to allow direct instantaneous comparisons to be made, a short selected sample was chosen from the experiment sampled at 10 kHz. The sample starts at a given time  $t_0$  and its length is 128 time steps, corresponding roughly to about five times the typical period  $T_p$  associated with the passage of structures (see Sect. 2.4). In order to allow for comparison between some of the applications of the different methods, we arbitrarily define a convention velocity  $U_c$  as  $U_c = 0.5(U_a + U_b)$ . The validity of this value can be disputed (Zaman and Hussain 1984); but, for the sake of uniformity, this value has been used by each contributor. We will denote  $x^*$  the spatial coordinate corresponding to the application of Taylor's hypothesis.

## 2.2

### Pseudo Flow Visualizations (PFV)

The use of dense rakes of probes combined with high speed simultaneous sampling is a way to determine accurately the

space-time evolution of the flow field (Glauser and George 1992), at least for the large scale organization of the flow. The use of the instantaneous reconstruction to analyze the behavior of the flow is not a new idea. Townsend (1979) and Browand and Troutt (1985) applied this concept to the instantaneous velocity profiles or time histories to help in analyzing the behavior of the flow. Delville et al. (1989) applied this approach to velocity signals in order to create "pictures" of the flow. The Pseudo-Flow-Visualization (PFV) technique allows one to simply handle a large amount of data, highlighting the large scale organization of the flow by simply considering the raw velocity signals. This approach can be compared with conventional experimental visualization techniques but avoids the problems due to seeding effects. Here the velocity field itself is considered as a "marker" of the flow. To get information on the spatial organization in the  $X$  direction, Taylor's hypothesis is used. Figure 4 gives some examples of such PFV's obtained from the Data Base. A more detailed description of the potential of this technique can be found in Bellin et al. (1993).

### 2.2.1

#### Global organization of the flow

The large scale organization of the flow can be characterized by the  $\omega_z = -\partial u/\partial y + \partial v/\partial x$  component of the vorticity. The footprint of this vorticity can be analyzed by considering the distribution of this quantity in the  $(x^*, y)$  plane. Simpler analysis can be performed by looking only at the time histories of the  $u$  or  $v$  component of the velocity in the  $(x^*, y)$  plane. Then considering variations in the  $y$  direction of the  $u$  component or the variations in the  $x^*$  direction of the  $v$  component will provide information on the large scale organization. Such a typical visualization is shown in Fig. 4, where the quantity  $v(y, t)$  is taken from the experiment with a sampling frequency ( $f_s = 100$  kHz). This PFV is obtained by applying a very simple coloration rule to the instantaneous velocities. The dark grey colors represent negative fluctuations, and the light grey

Table 1. Main characteristics of the experiments

Probes		Flow characteristics			
$N_p$	Spacing (mm)	Location (mm)	$x$ (mm)	$\delta_\omega$ (mm)	$R_\omega = \Delta U \delta_\omega / \nu$
12	$\Delta Y = 6$	$y = -33, -27, \dots, 33$	600	27.8	34 000

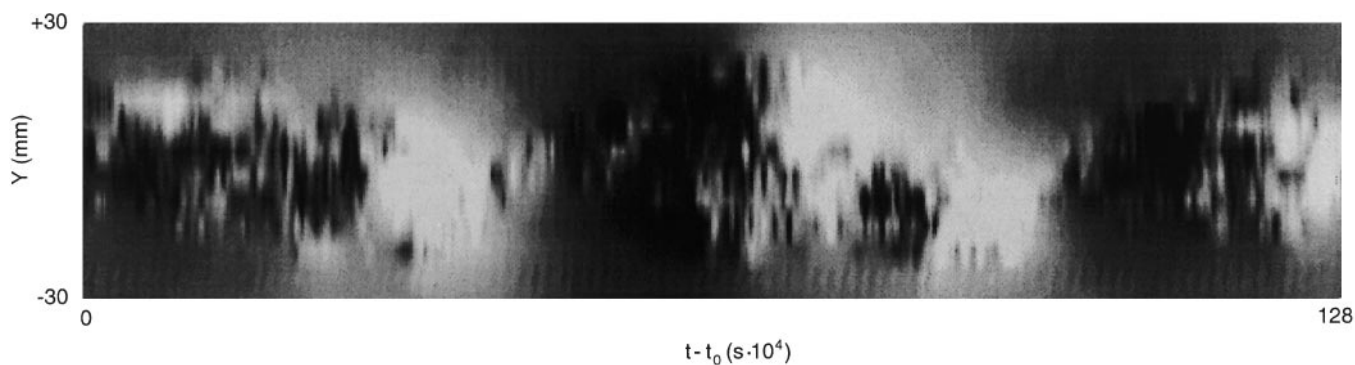


Fig. 4. Example of pseudo-flow-visualization. Dark gray areas matches to negative fluctuations and light gray areas to positive ones.

Raw  $v'$  plots ( $f_s = 100$  kHz)

colors represent positive fluctuations. The picture obtained is very similar to the one that might be obtained from conventional smoke visualizations. The passage of quasi-periodic large scale events are clearly evident. The period of occurrence of these patterns closely matches the peak-frequency  $f_p$  measured from the velocity spectra, as will be discussed in Sect. 2.4. The presence of tiny slanted links between the patches is evident. These links are very similar in shape and size to the braids.

### 2.2.2 Results on the selected short sample

Figures 5a–d show several PFV’s applied to the selected sample. Within these plots, time goes from left to right and  $x^*$  from right to left after using Taylor’s hypothesis. The coloration rule used in these PFV’s is based on the same concept as in the previous visualizations (light grey is positive, dark grey is negative). However, in order to add information about the intensity of the gradients, a saw-tooth rule is superimposed. In Fig. 5a, due to Hilberg (Bonnet et al. 1993), the width of the

bins for the  $u$  component is selected to be very narrow in order to visualize the perturbations mainly at large scale (Delville et al. 1989). In the mixing zone, the variation in time and space of the velocity makes it difficult to distinguish any pattern. In the external irrotational parts of the mixing layer large perturbations of fluid can be identified, suggesting the presence of braids. The PFV’s shown plotted in Figs. 5b and c correspond to the  $u'$  and  $v'$  local fluctuations respectively, while Fig. 5(d) shows vector-plots of the instantaneous velocity field ( $\bar{u} + u'$ ,  $\bar{v} + v'$ ), with the convective velocity  $U_c$  subtracted. In addition, the  $\omega_z$  contours and the instantaneous sectional streamlines are plotted for the selected sample, using the approach of Bisset and Antonia (see Sect. 7).

From these various representations, the notion of large scale structure convected by the mean flow is clearly evident. The main organization of the flow can be thought of as the succession of quasi spanwise aligned vortices convected by the mean flow. When structures are passing at fixed location, the  $v$  component of the velocity tends to evolve in phase over the mixing layer extent, introducing a global motion of fluid

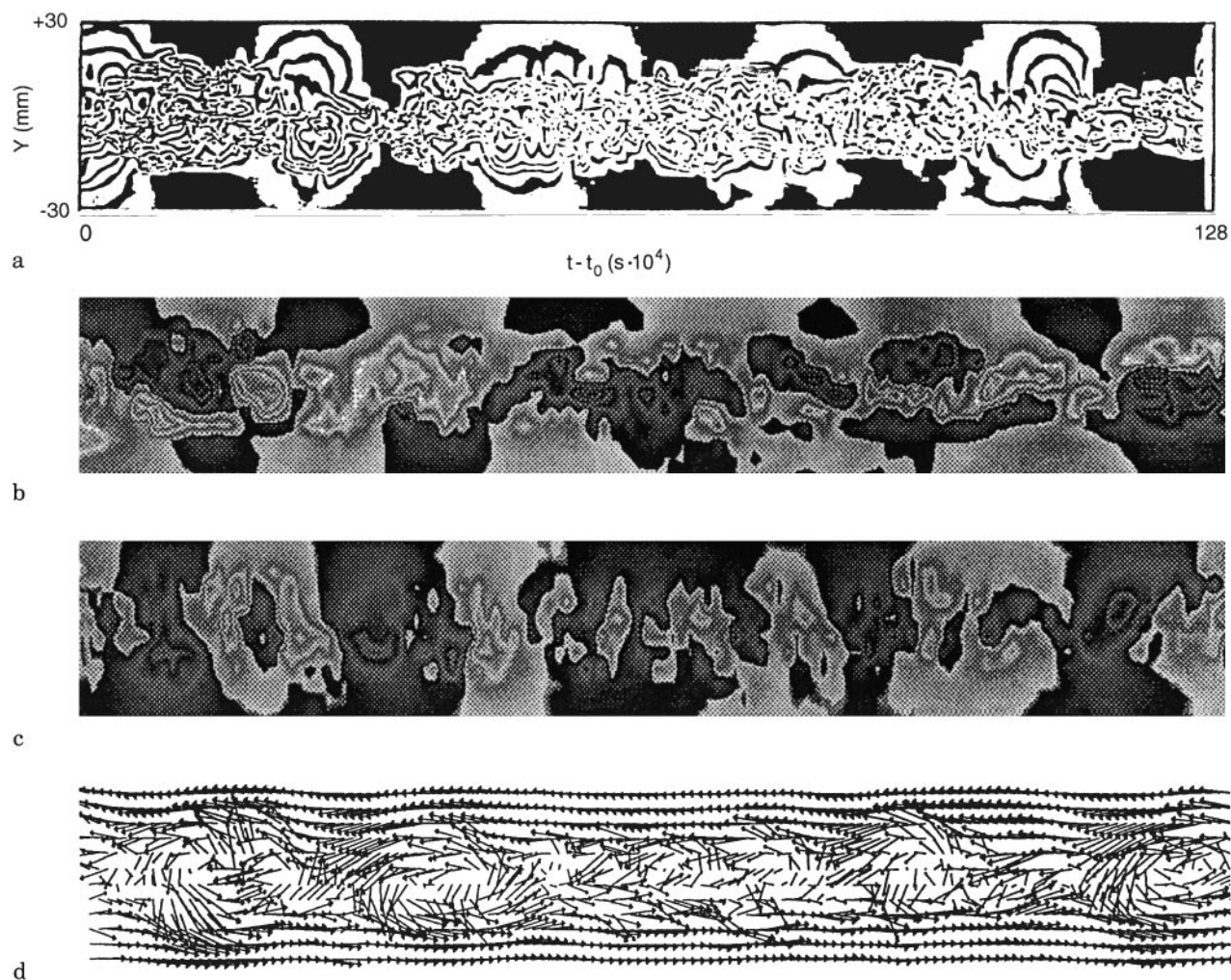


Fig. 5a–d. Pseudo-flow-visualizations for the selected sample. Dark gray areas matches to negative fluctuations and light gray areas to positive ones. a Iso-values of the “perturbations” of the longitudinal

velocity (from Hilberg); b iso-values of  $u'$ ; c iso-values of  $v'$ ; d velocity vector plot

going alternatively towards the lower velocity side and towards the upper velocity side. Moreover, even in the mixing zone, the footprint of the passage of a structure remains clearly visible. For the  $u$  component, the passage of these vortices can be detected mostly in the external parts of the mixing layer. It corresponds to a local increase of the velocity in the upper part of the flow and to a decrease in the lower part. This feature has been the basis of a large number of detection criteria (Tso and Hussain 1989, Browand and Weidman 1976) or Sect. 4.3 in this paper. However, for the longitudinal velocity component, the passage of the large scale structures is more difficult to detect in the mixing zone because the change in sign of  $u$  occurs somewhere within the structure's life-cycle and then is smeared by fluctuations over a wide range of scales inside the structure itself. This general behavior is illustrated by the results obtained for the  $u$  or  $v$  spectra discussion in Sect. 2.4.

### 2.3 Topology structures

Topology theory investigates the flow field in the vicinity of critical points, where the velocity vector  $c = \{u, v, w\}$  vanishes. At these singularities, the direction of the flow field is indefinite. The vector field in the proximity of the singularity with radius vector  $r(x, y, z)$  can be expressed by a Taylor series (refer e.g. Kaplan 1958; Hunt et al. 1978; Pery and Chong 1986) as

$$c = r \text{grad}(c),$$

where terms of higher order are neglected. The eigenvalues of the gradient  $\text{grad}(c)$  are important for the classification of the critical points assuming that the eigenvalues are non-zero. Otherwise terms of higher order determine the local flow characteristics. The non-trivial solution of the above linearized formulation is an eigenvalue problem

$$(\text{grad}(c) - \lambda \delta_{ij}) r = 0 \text{ with } r \neq 0$$

where  $\delta_{ij}$  denotes the Kronecker symbol. For the two-dimensional case, the eigenvalues are calculated by

$$\det(\text{grad}(c) - \lambda \delta_{ij}) = 0 \Leftrightarrow \lambda^2 - p\lambda + q = 0$$

$$\Leftrightarrow \lambda_{1,2} = \frac{1}{2}(-p \pm \sqrt{p^2 - 4q})$$

$$p = \lambda_1 + \lambda_2 = \frac{\partial u}{\partial x} + \frac{\partial v}{\partial y} \quad \text{and} \quad q = \lambda_1 \lambda_2 = \frac{\partial u}{\partial x} \frac{\partial v}{\partial y} + \frac{\partial u}{\partial y} \frac{\partial v}{\partial x}$$

From the resulting eigenvalues the corresponding eigenvectors, which determine the flow field in the vicinity of the critical

point, can be calculated. Classification of the topology structures is given by Hunt et al. (1978). For the plane flow, where  $p = 0$ , due to continuity, the region of a vortex point is described by complex eigenvalues with  $q > 0$ ; and the domain of a saddle point is given by the real eigenvalues with  $q < 0$ . As suggested by Dahlmann (1990), the area of a vortex structure is encircled by the dividing line between both singularities as the isoline, where the imaginary fractions of the eigenvalues are vanishing. This isoline can be calculated from

$$p^2 - 4q = 0$$

so that, the enclosed region of negative argument of the root indicates the vortex structure.

This criterion was used to determine the vortex regions in the mixing layer. Although only the  $u$ - and  $v$ -components of the velocity field were given, we recognized the three-dimensional flow by also considering the trace  $p$  of the characteristic matrix. All streamwise derivatives  $\partial/\partial x$  were obtained by application of Taylor's hypothesis with constant convection velocity. Figure 6 shows the results as hatched areas indicating the vortex areas. We can see that these areas are almost identical with the iso-vorticity planes displayed in Figure 15(a) from Sect. 4.3. As the comparison with the vorticity plot shows, regions of spatially correlated vorticity can be determined better than from only the vorticity distribution since the braid region, as a saddle point area, is not being viewed. These so-called inner-structures are concentrated in the larger flow patterns, or in other words, the coherent structures consist of two or more vortex areas. Therefore, we can clearly distinguish between vortex-free areas and regions of vortex concentration to determine the large-scale flow patterns. In addition, the criterion applied has the advantage that it is unequivocal in contrast to an arbitrarily defined iso-vorticity line.

### 2.4 Results from spectral analysis

The footprint of the large scale vortices that are known to occur quasi-periodically can, to some extent, be retrieved from the temporal signals of the velocity. As seen in Sect. 2.2, this foot-print is strongly related to the variations of the sign of the local velocity fluctuation and will be retrieved, in a statistical sense, from the frequency spectra distributions. The evolution of the  $u$  and  $v$  velocity spectra across the mixing layer are plotted on the axis and off the mixing layer axis in Fig. 7a. Note the difference in the behavior of these spectra. For the  $v$  component, a very well-defined narrow band peak of frequency appears in the spectra regardless of the location within the flow: i.e., this peak can be observed in the mixing area as well as in the outer parts of the mixing layer. On the

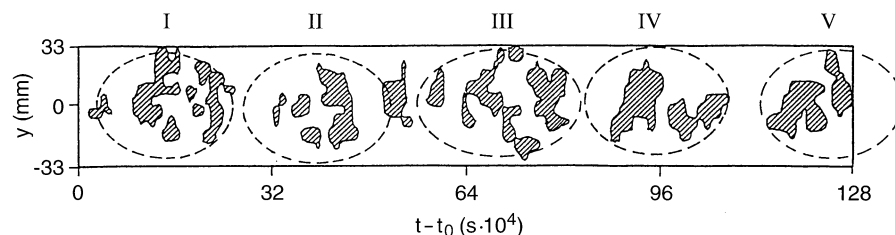


Fig. 6. Vortex areas determined by topology. Dashed lines show approximately large vortex regions

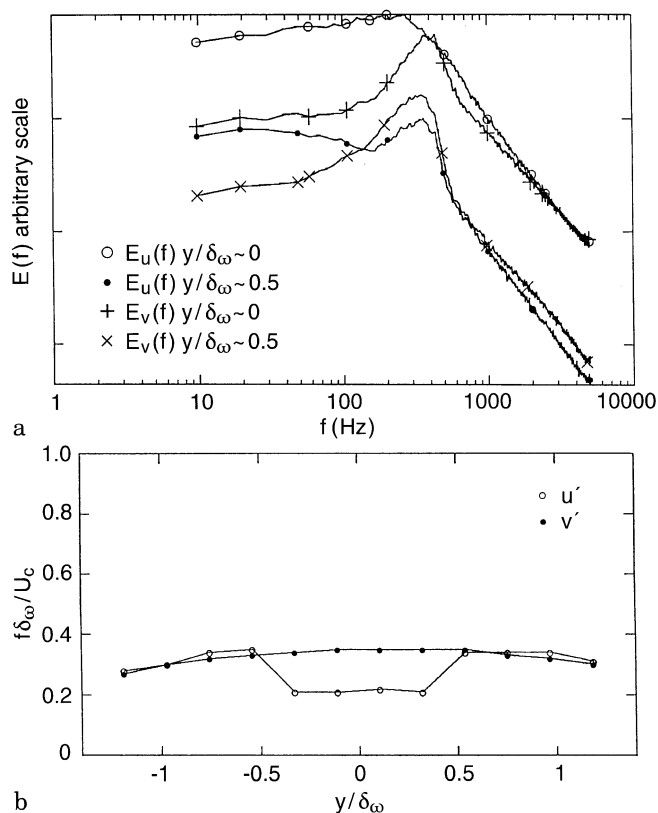


Fig. 7. a Fourier analysis of velocity components  $u'$  and  $v'$ , on the axis ( $y/\delta_w=0$ ) and on the middle of the mixing layer ( $y/\delta_w=0.5$ ); b Strouhal numbers based on  $u$  and  $v$  velocity components

other hand, for the  $u$  component, a narrow band of peak frequency can be retrieved only in the external parts of the mixing layer. In the center of the mixing zone, the dominant frequency is located at lower frequencies and is much more broad band. This behavior is illustrated in Fig. 7b, in terms of Strouhal number evolution across the mixing layer. The Strouhal number is based on the dominant frequency  $f_p$  observed from each spectrum (corresponding to the maximum of energy), the vorticity thickness and on the convective velocity  $U_c = (U_a + U_b)/2$ . These frequencies, which are *a priori* related to the same phenomenon, are strongly dependent on whether the  $u$  and  $v$  velocity spectra are being observed. Within the mixing zone ( $|y/\delta_w| < 0.5$ ) the Strouhal number remains stable but can be quite different, depending on the observed velocity component: 0.21 for the  $u$  component and 0.33 for the  $v$  component. These Strouhal numbers are comparable at the edges of the mixing layer ( $|y/\delta_w| \simeq 0.5$ ) where they have a value of 0.33. In the external part of the flow ( $|y/\delta_w| > 0.5$ ), the typical frequencies for the  $u$  and  $v$  components evolve in the same way, slowly decreasing the farther one proceeds out from the axis of the mixing layer. This decrease can be related to the fact that the farther one probe out from the axis probe is from the axis, the more it is statistically influenced by vortices of large size (smaller Strouhal numbers).

These observations illustrate the difficulty in providing a unique global definition of a characteristic time scale describing the large scale behavior, particularly for the plane

mixing layer. The information obtained from spectral analysis cannot be used for the analysis of the instantaneous behavior of the flow due to the non-local character of Fourier analysis. However, the evolution of the typical scales obtained in this preliminary study shows that particular locations have to be chosen within the flow in order to characterize the large-scale behavior. Based on the typical frequencies obtained across the mixing layer, a convenient and objective (in a statistical sense) location for defining the structure's passage could be the mixing layer edge, where both the  $u$  and  $v$  spectra collapse. This corresponds to the typical detection location used when fixed detector schemes are implemented.

### 3 Wavelet analysis

#### 3.1 The wavelet transform

The statistical picture of turbulence as “colored noise”, a collection of random velocity fluctuations with a particular energy spectrum has been largely superseded. It is now recognized that the phase-correlated vortical structures within a single realization determine many properties of the turbulence (e.g. peak concentrations of a pollutant spreading in a turbulent flow). In order to understand the role of these coherent structures in turbulence, one requires experimental and mathematical tools capable of detecting and analyzing such structures.

The Fourier transform analyzes the velocity signal into delocalized sine waves of particular wavelengths, amplitudes and phases and allows the definition of an energy spectrum; and, by Fourier transforming the Navier-Stokes equations, dynamical spectral quantities such as the exchange of energy between wavenumbers may also be defined. The Fourier transform is, however, not that well suited for analyzing the coherent structures within a single turbulent flow because its basis functions (the dilated sine waves) are perfectly localized in wavenumber space; and, thus, by the uncertainty principle they are completely delocalized in physical space. The Fourier transform hides physical space information. In order to understand the function of physical eddies in the energy cascade and other turbulence processes, we require a way of analyzing the velocity field that preserves some degree of localization in both physical and wavenumber space.

The wavelet transformation is a mathematical tool which is capable of providing simultaneously both a wavenumber and a physical space analysis. Several applications of wavelet transforms have been devoted to the analysis of turbulent flows (e.g. Farge 1992, Lewalle 1994). In this section we show how the wavelet transform may be used to detect and analyze coherent structure in a turbulent flow. Grossman and Morlet introduced the wavelet transform in 1984. In the wavelet transform a signal is broken down into a family of localized ‘wavelets’ which are obtained by translating and dilating a mother wavelet  $\psi(x)$  in such a way that the wavelets remain self-similar. The parameters of the wavelet transform are a location  $x_0$  for the translation and a scale  $a$  for the dilation. The wavelet is defined by

$$\Psi(x, x_0, a) = a^{-1/2} \psi\left(\frac{x - x_0}{a}\right) \quad (1)$$

where the factor  $a^{-1/2}$  ensures that the wavelet energy  $a^{-1} \int \Psi(x, x_0, a) dx_0$  is conserved at each scale. A function  $\psi(x)$  can be a 'mother' wavelet if it is well localized in both physical and wavenumber space and is *admissible*. The first requirement means that the wavelet's spread in  $x$ -space is given by a finite constant  $\Delta x = \sigma$ , and its spread in  $k$ -space is given by  $\Delta k = 1/\sigma$  (from the uncertainty principle  $\Delta x \Delta k \geq 1$ ). Because of its self-similarity, the wavelet's spread in physical space is  $\sigma a$ ; its spread in wavenumber space is  $1/(\sigma a)$ ; and its norm scales like  $a^{-1}$ . Thus, the wavelet transform resolves the small scales finely and the larger scales more coarsely.

The admissibility requirement means that the wavelet must satisfy

$$C_\psi = 2\pi \int_{-\infty}^{\infty} |\hat{\psi}(k)|^2 \frac{dk}{k} < \infty \quad (2)$$

where  $\hat{\psi}(k)$  is the Fourier transform of  $\psi(x)$ . This requirement means that the wavelet must have zero mean and ensures that a reconstruction formula exists for the wavelet transform. Practically, these two conditions mean that one chooses a mother wavelet which is an oscillating function (wavenumber space localization) about zero with a rapidly decaying envelope (physical space localization).

The one-dimensional continuous wavelet transform  $\tilde{u}(x_0, a)$  of a function  $u(x)$  is then defined as

$$\tilde{u}(x_0, a) = a^{-1/2} \int_{-\infty}^{\infty} u(x) \psi^* \left( \frac{x - x_0}{a} \right) dx \quad (3)$$

Thus the wavelet transform allows one to investigate simultaneously the structure of a signal in both physical and wavenumber space. The wavelet transform acts like a mathematical microscope in which the optical characteristics are determined by  $\psi$ , and  $a^{-1}$  is the magnification at the focal point  $x_0$ .

The wavelet transform is ideally suited to the investigation of coherent structures in turbulence because it allows the definition of the *local* 'energy spectrum'

$$W(x_0, a) = |\tilde{u}(x_0, a)|^2 \quad (4)$$

By integrating the local energy spectrum  $W(x_0, a)$  over a coherent structure it is possible to find the energy spectrum associated with that particular structure. The energy spectrum of the coherent structure may then be compared with the wavelet energy integrated over the whole flow  $E_w(a)$

$$E_w(a) = \frac{1}{L} \int_0^L |\tilde{u}(x_0, a)|^2 dx_0 \quad (5)$$

(analogous to the Fourier energy spectrum) to determine how that structure contributes to the energy spectrum of the flow as a whole. This technique may help us to determine which structures in the physical space (if any) are responsible for the  $k^{-5/3}$  energy spectrum of the inertial range of turbulence.

The wavelet transform can also be used to *detect* coherent structures in turbulent flows. Approximate singularities in the flow (such as produced by spiral vortices, i.e. vortices made up of wound-up vortex sheets) appear in the  $(x_0, a)$  plane of the wavelet transform as long, slender cones pointing towards the location  $x_0$  of the structure. Strong, isolated cones in the

wavelet transform are, therefore, the signature of eddies or other approximately singular structures in the flow. By examining the rate of the decay of the wavelet transform with  $a$ , it is also possible to determine the order of the structure's singularity (Bacry et al. 1990). Coherent structures in a turbulent flow can thus be both detected (by looking for cones) and characterized (by finding the order of singularity and local energy spectrum) using the wavelet transform.

The wavelet transform can generate statistics showing how the energy spectrum (or transfer of energy) varies from place to place in the flow (e.g. Meneveau 1991). A useful quantity measuring the spatial fluctuation of wavelet energy is its standard deviation

$$S_w(a) = \left[ \int_0^L (\tilde{u}^2(x_0, a) - E_w(a))^2 dx_0 \right]^{1/2} \quad (6)$$

The spatial fluctuation of the wavelet energy is related to intermittency (high intermittency will produce a high fluctuation, but the converse is not necessarily true) and measures how spatially homogeneous the energy is at different length scales. By plotting the percentage standard deviation of wavelet energy,  $I_w(a) = S_w(a)/E_w(a) \times 100$ , as a function of  $2\pi/a$  one can get an idea of how evenly the energy is distributed at different wavenumbers.

We analyze the mixing layer data using the complex-valued Morlet wavelet

$$\psi(x) = \exp(ik_0x) \exp(-\frac{1}{2}|x|^2) \quad (7)$$

(where  $k_0 = 6$  to make the wavelet admissible within computer round-off error). The Morlet wavelet is selected because the resulting spatially averaged wavelet energy spectrum is usually very close to the Fourier energy spectrum (e.g. same power-law) making comparison with traditional methods straightforward.

The continuous wavelet transform is actually computed in Fourier space using the relation

$$\hat{\tilde{u}}(k, a) = a^{-1/2} a \hat{\psi}(ak) \hat{u}(k) \quad (8)$$

where  $\hat{(\ )}$  indicates a Fourier transformed quantity, and the Fourier Transform of the Morlet wavelet is

$$\hat{\psi}(k) = \sqrt{\pi} \exp(-(k - k_0)^2/4). \quad (9)$$

The Fourier space version of the wavelet transform at each scale is then transformed to physical space using the FFT. This method of computing the wavelet transform brings out the role of the wavelet as a sort of Fourier-space filter and is much more efficient than carrying out the convolution in physical space. This method is ideal for a structural analysis since an arbitrary number and distribution of scales can be chosen (unlike the discrete wavelet transform of Mallat (1989) in which the scales and positions are arranged in a fixed, dyadic hierarchy).

In the next section, the cones in the one-dimensional wavelet transform are used to detect structures in the low resolution  $y$ -aligned rake mixing layer velocity data. The percentage standard deviation as a function of  $a^{-1}$  is measured at various transverse positions to investigate how energy inhomogeneity changes across the mixing layer.

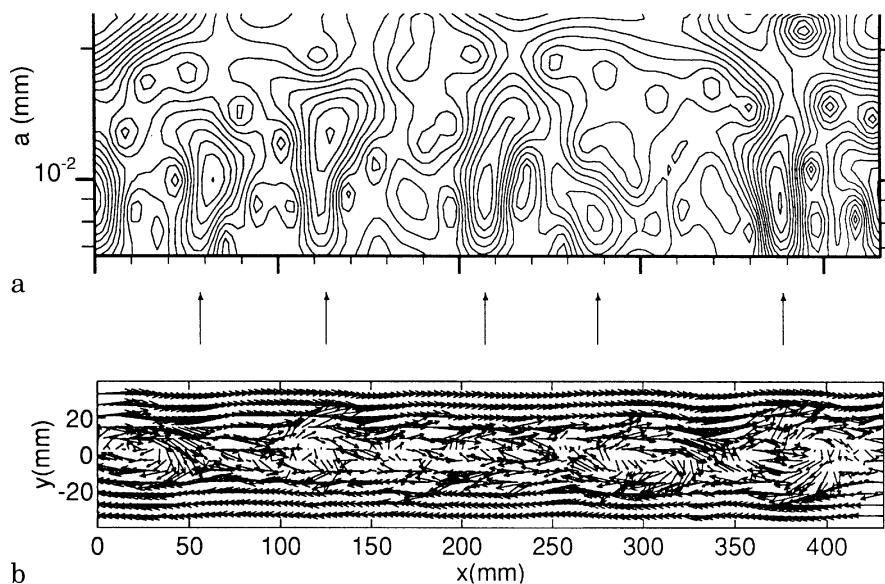


Fig. 8. **a** Modulus of the wavelet transform of transverse velocity at  $y = -3$  mm (only the smaller length scales are shown). Arrows show the location of strong cones which are associated with eddies in the mixing layer. **b** Velocity vectors in mixing layer from  $y$ -aligned rake (time runs from right to left)

### 3.2

#### Structure detection and spatial fluctuation of energy

In this section, data from the  $y$ -aligned hot-wire rake is analyzed using the one-dimensional wavelet transform to show how structure may be detected and how the spatial fluctuation of wavelet energy as a function of inverse length scale varies across the mixing layer.

Figure 8a shows a contour plot of the modulus of the wavelet transform of 128 points of the  $v$  (transverse) velocity at  $y = -3$  mm. By comparing Fig. 8a with the plot of the velocity vectors in Fig. 8b one can see that the strong 'cones' in the wavelet transform (indicated by arrows) point to the location of the centres of the eddies or (less commonly) to the saddle-points (irrotational straining regions) between eddies. The fact that cones in the modulus of the wavelet transform are associated with eddies in the mixing layer indicates that eddies are flow structures whose activity extends down to very small length scales. Because cones in a wavelet transform are associated with singularities in the original signal, one may consider the large eddies of the mixing layer to be approximate singularities of the flow. These results indicate that the appearance of strong cones in the wavelet transform of a turbulent velocity signal may indicate the location of strong coherent structures. Since we have only taken a one-dimensional slice through the mixing layer, it is difficult to distinguish between eddy and saddle-point type coherent structures, both of which create cones because of their strong gradients and large range of length scales.

Another question that may be asked is: how does the presence of the large mixing layer eddies affect the way inhomogeneity of energy varies with length scale? In Fig. 9(a) the average wavelet energy spectra at  $y = 33$ , 15 and 3 mm is plotted (note the roughly  $k^{-5/3}$  range at  $y = 15$  and 3 mm and the much more rapid decay at  $y = 33$  mm); and in Fig. 9b the percentage standard deviation as a function of inverse length scale is plotted at the same three transverse locations. Note that in all three cases the level of fluctuation increases monotonically with  $a^{-1}$  (energy at the small scales is more unevenly

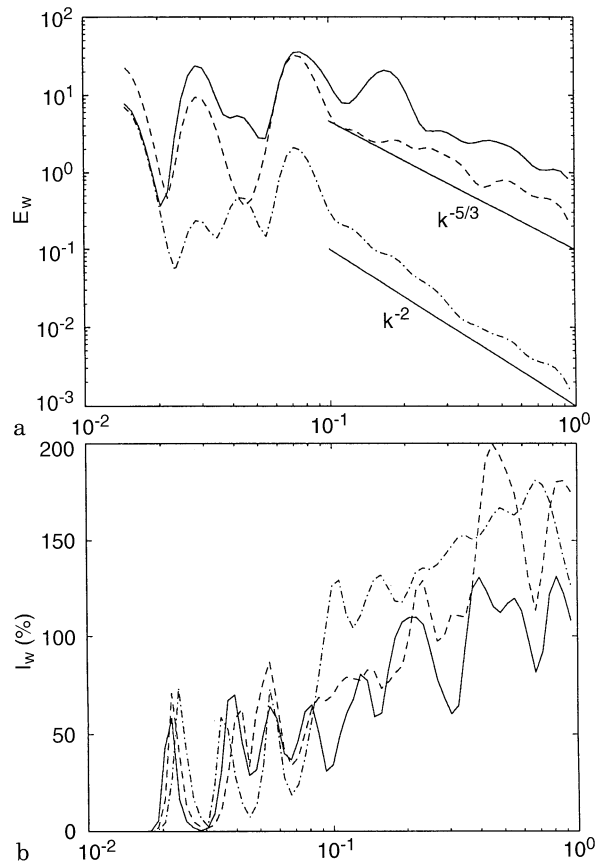


Fig. 9. **a** Spatially averaged wavelet spectra of transverse velocity at  $-y = 3$  mm,  $-y = 15$  mm and  $-y = 33$  mm compared with a  $k^{-5/3}$  spectrum. **b** Percent standard deviation of wavelet energy at the same transverse positions as (a). Note the lower energy fluctuation at small scales near the axis of the mixing layer

distributed), but that this increase is *slower* for probe positions closer to the axis of the mixing layer. The increase in  $I_w$  at the smaller length scales may be the result of an increasingly intermittent distribution of kinetic energy at these scales.

Qualitatively similar behaviour of the energy fluctuation is seen for the low-velocity side and for the streamwise velocity component.

Note that the averaged wavelet spectra are much smoother than the equivalent Fourier spectra would be. This smoothness comes from the averaging in physical space over many locations and from an effective averaging in wavenumber space because of the finite width of the Fourier transform of the Morlet wavelet. The smoothness of the spatially averaged wavelet energy spectrum is an advantage over the Fourier energy spectrum for analyzing individual realizations of the flow (to investigate the role of coherent structures one must look at individual flow realizations and not ensemble averages).

The energy fluctuation at small scales is lowest near the axis of the mixing layer because that is where the coherent structures (eddies and straining regions) responsible for the small scale energy are the most dense. Note from Fig. 9b that there is little change in the level of fluctuation at the large scales, indicating that the coherent structures of the mixing layer have a spatially uniform distribution of energy at the small scales. The large scale eddies of the mixing layer are thus seen to smooth out the energy of the small scales. This is in contrast to the small (approximately Taylor scale) 'worms' observed in DNS turbulence which are thought to be at least partially responsible for the small scale intermittency of turbulent (Jiménez et al. 1993).

The efficiency of the Wavelet method in educing coherent structures from this flow will be discussed later. However, from this application, it can be inferred that the method in its present form is not efficient, mainly because it only uses the information obtained at a single location so that the results are strongly dependent on the location of the detector. More recent *work in progress* involves a global use of Wavelet analysis which takes advantage of the knowledge of the entire flow information (Bonnet et al. 1996). It is clear from these results that additional work is needed for the application of the Wavelet transform for coherent structure eduction from real data.

## 4

### Proper orthogonal decomposition

#### 4.1

##### The proper orthogonal decomposition

The POD was proposed by Lumley (1967) as an unbiased way for extracting structures from turbulent flows. He suggested that the coherent structure be the structure that has the largest mean square projection on the velocity field. This maximization leads to a Fredholm integral value problem, where the kernel is the two-point correlation tensor.

In the present study, only the  $y$  (mean gradient or inhomogeneous) direction is considered. Of course this approach is limited by the fact that the three-dimensional aspects of the flow cannot be accessed since only one slice of the flow is viewed here. However, useful information on the global organization of the flow can be outlined.

Following the approach of Lumley (1967), the dominant structures of the flow can be determined from the following

equation:

$$\sum_{j=1}^{nc} \int_{\mathcal{D}} \Psi_{ij}(y, y'; f) \Phi_j^{(n)}(y'; f) dy' = \lambda^{(n)}(f) \Phi_i^{(n)}(y; f), \quad (10)$$

where  $nc$  is the number of velocity components on which the POD is performed and where the cross-spectral tensor  $\Psi_{ij}(f)$  is the temporal Fourier transform of the two-point space-time correlation  $R_{ij}(y, y'; \tau) = \langle u_i'(y, t) u_j'(y', t + \tau) \rangle$  (corresponds to conventional average). In the present study, the number of components  $nc$  is 2 and a vectorial approach is used. This application of the POD will be noted  $POD_f$ .

A simpler approach is also performed in the present section; in this case, the time dependency is not taken into account. The kernel of the Fredholm equation is the spatial correlation tensor; and the equation to be solved is

$$\sum_{j=1}^{nc} \int_{\mathcal{D}} R_{ij}(y, y'; \tau=0) \phi_j^{(n)}(y') dy' = \Lambda^{(n)} \phi_i^{(n)}(y) \quad (11)$$

This application of the POD will be noted  $POD_n$ .

The eigenvectors  $\phi_i^{(n)}(y)$ , solutions of Eq. (11), can be used to reconstruct the velocities:

$$u_i(y, t) = \sum_n a_n(t) \phi_i^{(n)}(y) \quad (12)$$

where

$$a_n(t) = \sum_{i=1}^{nc} u_n(y, t) \phi_i^{(n)}(y) dy \quad (13)$$

With the first Eq. (10) the eigenvectors  $\Phi_i^{(n)}$  are frequency dependent and cannot be retrieved in the physical space ( $y, t$ ) because of the loss of temporal phase due to the non-local character of the Fourier transform in the physical space. However by using rakes of hot-wires, the instantaneous contribution of each mode of the  $POD_f$  can be retrieved by considering the following equations in Fourier space:

$$\widehat{u}_i(y, f) = \sum_n A_n(f) \Phi_i^{(n)}(y, f) \quad (14)$$

$$A_n(f) = \sum_{i=1}^{nc} \widehat{u}_i(y, f) \Phi_i^{(n)}(y, f) dy \quad (15)$$

where  $u_i(y, t)$  can then be obtained from the inverse Fourier transform.

The numerical procedure for solving the POD can be found in Glauser and George (1987). This procedure leads to the search for the eigenvalues and eigenvectors of a matrix of size  $N_m = nc \times N_y$ , where  $N_y$  is the number of spatial points in the  $Y$  direction. In these applications of the POD, the number of modes obtained is  $N_m = 24$ . For  $POD_f$ , the solution is performed for each frequency  $f$  independently, and the matrices are complex Hermitian. In the case of the  $POD_n$ , there is only one real symmetric matrix to deal with.

The kernel of Eq. (11) is in general a statistical quantity; and typically it is defined as a time, space or ensemble average. However, it is possible to define a kernel which is based on conditional averages. An application of the first definition is described in the Conventional POD section below. This is followed by a section which is devoted to an application of a Conditional POD.

## 4.2

### Conventional POD

In the first application, the POD takes into account only the spatial correlations. Later, the frequency dependency is added to the problem to be solved. The rates of convergence of these POD modes and the shapes of the dominant modes are analyzed. Finally, it is shown that both approaches give, for the dominant mode, a realistic description of the instantaneous temporal evolution of the flow.

#### 4.2.1

##### Convergence of POD modes

The eigenvalues are representative of the turbulent energy contained within the whole spatial domain on which the POD is performed. The energy contained in each mode of the POD is presented in Fig. 10. For the case of  $POD_f$ ,  $\mathcal{E}^{(i)} = \int \lambda^{(i)}(f) df$  is the energy contained in the entire flow field for mode (i), integrated over all frequencies. For the case of  $POD_n$ ,  $\mathcal{E}^{(i)}$  is the eigenvalue  $\Lambda^{(i)}$ . The energy contained in the first modes of the POD is given in Table 2. When considering these modes, the  $POD_f$  application provides a better reconstruction of the energy than the  $POD_n$  does. This is due to the fact that the  $POD_f$  is able to take into account the frequency behavior of the velocity and is more physically representative than the  $POD_n$  which takes only the spatial character of the flow into account.

The frequency distribution of the eigen-spectra  $\lambda^{(n)}(f)$  for the first three modes of the  $POD_f$  are plotted in Fig. 11. The rapid convergence of the POD is clearly evident here. The eigenspectrum corresponding to the first mode shows a maximum located near a typical Strouhal number  $f\delta_\omega/U_c$  of the order of 0.3, which is characteristic of the typical large scale vortices passage frequency as seen in Sect. 2. At this frequency, the ratio between the first and second mode is about 4; and the first mode contains more than 70% of the energy in this band of frequency. This shows that the application of  $POD_f$  is quite efficient in representing the large scale characteristics of the flow.

#### 4.2.2

##### Reconstructions of the selected sample

In terms of structure identification, the role of any mode in the instantaneous flow field can be reconstructed by using Eqs. (14) and (15) for  $POD_f$  or Eqs. (12) and (13) for  $POD_n$ . Figure 12 shows, for the selected sample, the instantaneous velocity field plotted in a frame moving with the convective velocity  $U_c$  and using the Taylor hypothesis based on  $U_c$ . The sample size is  $\tau U_c/\delta_\omega \simeq 20$  and corresponds to about five structures with a separation based on the typical Strouhal number  $St_\omega = 0.3$ . We apply here only the reconstruction obtained with the  $POD_f$ . The global characteristics of the organization which can be visually found from the original velocities (Fig. 12a) is relatively well reconstructed by the first mode (Fig. 12b). However the spatial extent of the events is generally underestimated and other modes are needed to improve this spatial estimation. This can be evidenced by comparing Fig. 12c, where a four mode representation is given, with the original result plotted in Fig. 12a.

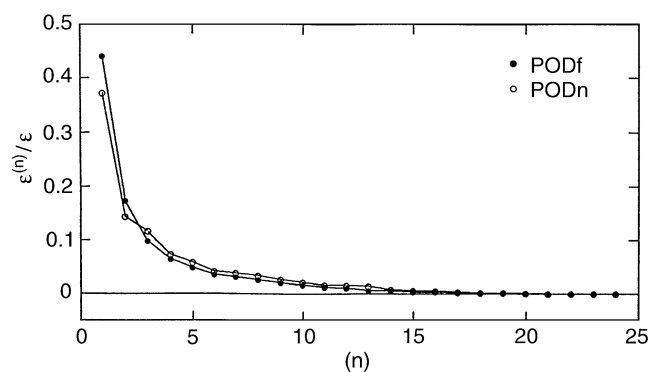


Fig. 10. Distribution of modes in the  $POD_f$  and  $POD_n$ . For the  $POD_f$  the energy is integrated over all frequencies

Table 2. Energy contained in the first modes of the  $POD_f$  and  $POD_n$

POD	Mode 1	Mode 2	Mode 3	First 3 modes
$POD_f$	44%	17%	10%	71%
$POD_n$	37%	14%	12%	63%

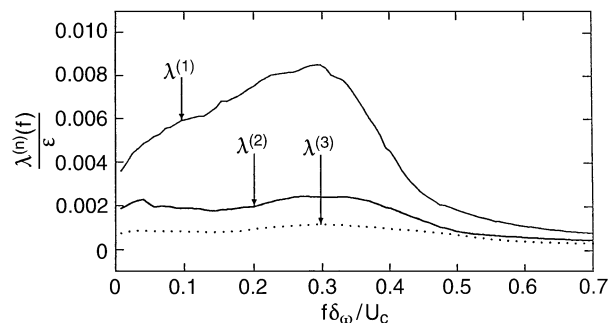


Fig. 11. First 3 Eigen-spectra frequency distribution for the vectorial  $POD_f$

#### 4.2.3

##### Shape of the eigenvectors

Due to the loss of temporal phase related to the use of the  $POD_f$ , the corresponding eigenvectors cannot be retrieved in the physical space  $(y, t)$  and can be described only in the Fourier space  $(y, f)$ . However, for each frequency the organization in the  $y$  direction remains meaningful. Hence, information on the organization of the flow can be obtained from the spectral distribution of  $\Phi_u^{(i)}$  and  $\Phi_v^{(i)}$  which are plotted in Fig. 13 for the first mode. On this plot, the modulus of the  $\Phi$  (which are complex functions) are shown. This modulus is weighted by the square root of the corresponding eigenvalue which results in units of velocity/Hz.

For all the frequencies, the eigenvectors exhibit some well-defined symmetries relative to the axis of the mixing layer  $(y=0)$ , as can be inferred from the symmetry of the energy profile. On the axis, the eigenvector  $\Phi_u$  has two maxima located at the frequencies  $f\delta_\omega/U_c = 0.16$  (A) and 0.5 (B), respectively. For the frequency  $f\delta_\omega/U_c = 0.32$ , two other maxima can be found for  $|y|/\delta_\omega \simeq 0.5$  (C and C'). The eigenvector  $\Phi_v$  has only

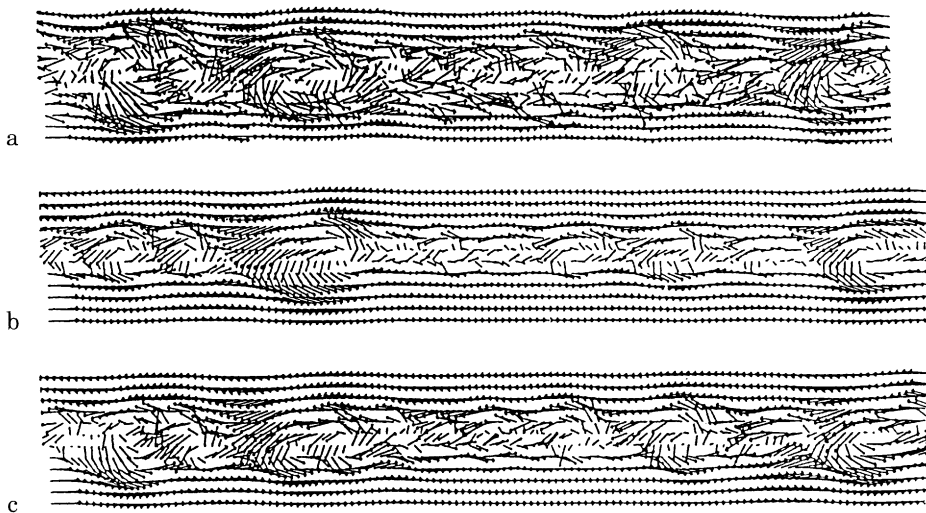


Fig. 12a–c. Contribution of first modes of the  $POD_f$  to the selected sample. **a** Original; **b** first model; **c** sum of the first four modes (same scales as for Fig. 5)

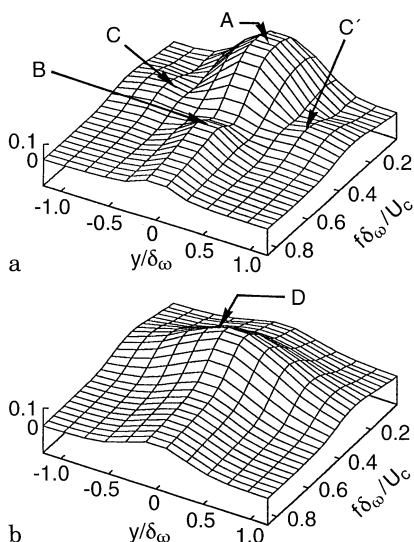


Fig. 13a, b. Shapes of the eigenvector for the  $POD_f$ . **a**  $\sqrt{\lambda^{(1)}(f)} \Phi_u^{(1)}(y, f)$ ; **b**  $\sqrt{\lambda^{(1)}(f)} \Phi_v^{(1)}(y, f)$

one maximum, located on the axis of the mixing layer and at the frequency  $f\delta_\omega/U_c = 0.32$  (D). For the  $\Phi_v$ , whatever the frequency, the order of magnitude of the imaginary part was found to be small when compared to the real part. This implies that the  $v$  component of the structure remains in phase over the  $y$  direction. The behavior of  $\Phi_u$  is quite different. For this last eigenvector, the order of magnitude of the real and imaginary parts are comparable. The real part of  $\Phi_u$  remains globally symmetric relative to  $y=0$  while the imaginary part is antisymmetric for the range of frequency around the location of the extrema (C) and (C'). This behavior implies that, for these frequencies, the eigenvectors are in phase opposition from side to side of the mixing layer axis. This behavior of the eigenvectors can be related to the “large scale” behavior of the flow.

From a conventional description of frozen convective 2D vortical structure, the passage of a structure can be associated

with an increase of the velocity in the rapid part of the M.L. which in turn is associated with a decrease of velocity in the slow part. This passage can then be related to a phase opposition between the two external parts of the mixing layer. This behavior expressed in terms of the eigenvectors can be translated into antisymmetrical behavior (odd function in  $y$ ). In complex space this behavior is related to a dominating odd imaginary part (in the  $y$  direction). The primary maximum at  $f\delta_\omega/U_c \simeq 0.15$  corresponds to symmetric real parts of the eigenvectors. This symmetry is related to the maximum of energy located on the axis of the M.L. is discussed in Sect. 2.

The first three eigenvectors  $\phi^{(m)}$  obtained from the  $POD_n$  are plotted in Fig. 14. For this application of the POD, the  $\phi$  are defined only in the  $y$  domain; and their analysis is easier to perform. A symmetric trend relative to  $y=0$  appears as was the case for  $POD_f$ . For both components  $u$  and  $v$ , the first and third mode of  $POD_n$  are even functions of  $y$  while the second mode is an odd function. Hence, the first mode of the  $POD_n$  can only translate velocity profiles which are even, and the second mode is necessary to be able to translate odd organization. This result may explain why the first mode of the  $POD_n$  is less representative than the first one from  $POD_f$ .

We have presented two applications of the POD to the data acquired in the plane mixing layer. The first application uses the cross-spectral tensor as the kernel for the Fredholm equation while the second application uses only the spatial correlation tensor. The use of the cross-spectral tensor for the kernel is more efficient at representing the large scale structure of the flow than the use of the spatial correlation tensor. Examination of the eigenvectors for the first POD model shows that the dominant mode is representative of the major flow characteristics known to exist in this flow.

### 4.3

#### Further applications of the POD

This section presents an additional application of the conventional POD which examines the contributions of the POD modes to the vorticity. This particular application is then used

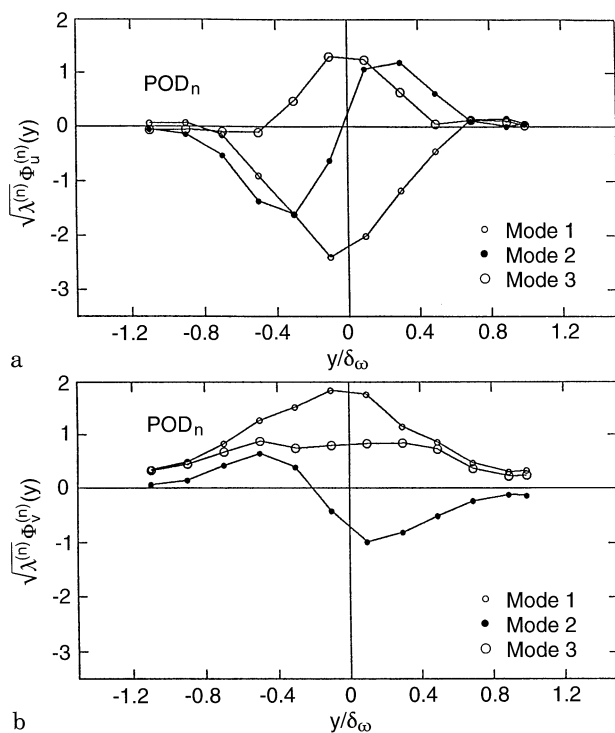


Fig. 14a, b. Shapes of the first eigenvectors for the  $POD_n$ . a First modes of  $\Phi_u(y)$ ; b first modes of  $\Phi_v(y)$

as a guide in implementing the conditional approach as described below.

#### 4.3.1 Additional applications of conventional POD

Figure 15(a) shows isolines of the vorticity component  $\Omega_z = \partial v / \partial x - \partial u / \partial y$  derived from the velocity field. In order to obtain the spanwise gradient  $\partial v / \partial x$ , Taylor's hypothesis with a spatially constant transport velocity was used. In general, the large vortices consist of two or more areas of encircled isolines.

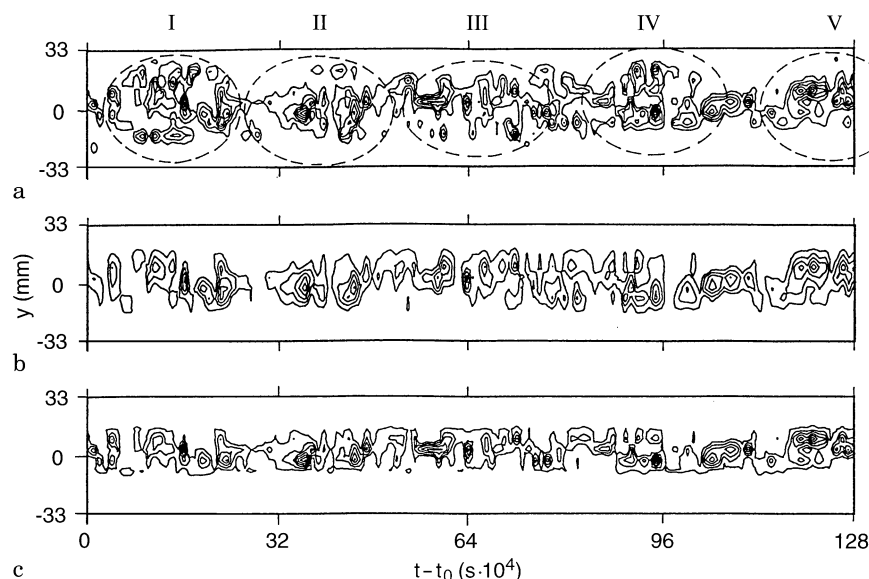


Fig. 15a–c. Isolines of the derived vorticity field. Dashed lines show approximately large vortex areas labeled by roman digits. a Original data; b derived vorticity field from the reconstructed flow field of the first three velocity based POD-modes; c Reconstructed by use of the first three vorticity based POD-modes

The enclosing isoline of the large structure usually has low values in comparison with maxima found in the inner region. Therefore, areas of vorticity correlated with the large structures found by the detection method described below are approximately indicated by dashed lines. The vorticity field calculated from the reconstructed velocity field of the first three POD modes is shown in Fig. 15b. Significant peaks are smudged, but the global behaviour is clearly evident, indicating that the principal flow field is included in the energy containing modes. If the POD is applied directly to the vorticity data, the reconstruction of the vorticity field (Fig. 15c) is not as well reconstructed by the lower modes. The reconstructed field of the first three modes, which contains about 60% of the total quadratic enstrophy, also embodies the maxima of the vorticity but only in the inner area of the shear layer. The outer field is not defined by these modes because in this region the components of the correspondent eigenvectors are close to zero. The decomposition scheme maximizes the spatially correlated quadratic enstrophy which is represented in the first modes. Since most of the enstrophy is concentrated in the inner region of the mixing layer, large areas of relatively weak but correlated vorticity – as a loose definition of coherent structures – are represented by the higher modes. Therefore, the first few modes from the application of POD to the velocity field contain the major characteristics of the large structures since the energy is spread over a wider area in the mixing layer.

#### 4.3.2 Conditional POD

Selected structures of the flow can be understood as so called *snapshots* of flow patterns. The usual way to extract their mean behaviour is the average of the ensemble. The POD allows one to decompose the snapshots into a number of energy containing modes and to calculate typical eigenflows.

A simple method was used to extract the snapshots. It is well known that large structures in the shear layer leave a *footprint* as potential fluctuation in the outer flow. By plotting the absolute velocity  $|c'|$  measured by the first probe in the low

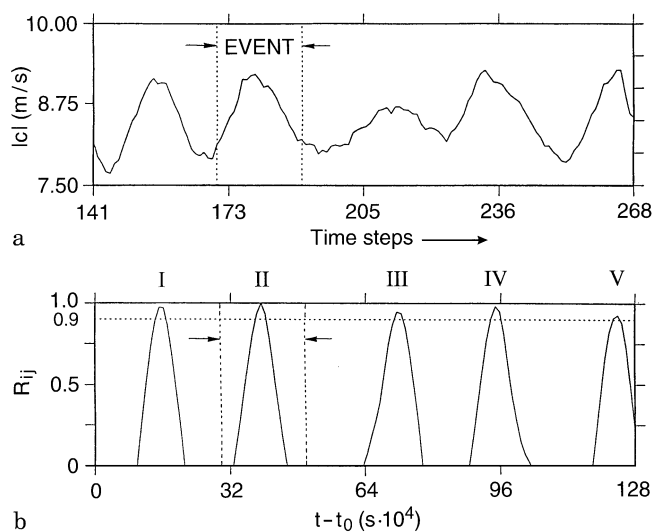


Fig. 16. **a** Absolute value of the velocity measured by probe no. 12 ( $y=33$  mm) in the irrotational high speed flow, whereas transport velocity was subtracted. Roman digits denote typical expirations. A typical event was selected (no. *II*) and correlated with the total signal; **b** The correlation function shows high maxima

velocity stream, one can identify typical fluctuations of this footprint (Fig. 16a). By scanning a selected representative distribution as correlation trigger over the entire signal, the resulting correlation shows typical maxima in the range  $0.65 < R_{cc} < 1.0$  (Fig. 16b). The respective maximum indicates the center of the individual flow pattern. If the flow patterns can be seen as *frozen* snapshots, the time-coordinate can be transformed into the streamwise direction. The interval of the snapshots is selected to be  $\pm 16$  time steps off the center. The method detected 320, 296 and 243 structures by using the

boundaries  $R_{cc}=0.7, 0.8$  and  $0.9$ . Since the mean velocity field is not a typical feature of the individual snapshot, it was subtracted from the detected patterns. In order to draw the vector plots in the following, the mean velocity was added in each case. Choosing as threshold  $R_{cc}=0.9$ , the obtained 243 structures were averaged (Fig. 17a). This ensemble average shows a *smearred* single-vortex structure caused by the different types of structures sampled by the applied recognition method.

Application of POD onto the extracted flow patterns yields so-called eigenflows. They are almost identical with the coefficients  $a_m$ , but normalized with the largest component of the corresponding eigenvector. Here, the eigenvectors define the occurrence and participation of the correspondent eigenflows in the individual snapshot. The eigenflow with the largest energy content of about 18% is a single vortex (Fig. 17b). Eigenflows with decreasing eigenvalues exhibit a similar flow-field but with different spatial extensions and shifts. But also double-vortex structures within the first eight modes can be found (Fig. 17c). Considerably higher, less important modes have eigenflows with a larger number of vorticities.

By classifying the eigenflows into classes of single-, double- and multi-vortex structures, we found a total energy content of 44.4% for the single-vortex and 13.8% for the double-vortex type. A closer inspection of the eigenvectors shows that only the first mode has positive components without exception. All others exhibit stochastic fluctuations of relatively high amplitude in comparison to the first eigenvector. This reflects the meaning of the first eigenflow. In this case; the largest mode determines the outer shape of the structures – where the local influence is given by its particular component – while the less important eigenflows define the inner structure.

Individual snapshots can be reconstructed by POD modes. Figures 18a, b show the vortex no. V (ref. Fig. 17a) reassembled by use of the first *local* energy containing modes in comparison

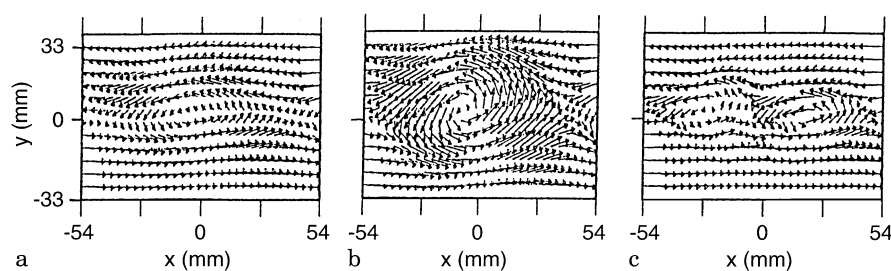


Fig. 17. **a** Ensemble average of detected "snapshots"; **b** first eigenflow showing single vortex structures; **c** example of double structure (eigenflow no. 8)

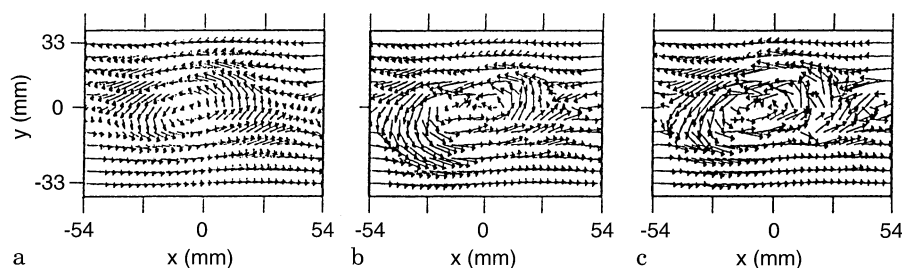


Fig. 18. Individual snapshot reconstruction. **a** First local energy containing mode of low pattern no. V (identical with first eigenflow); **b** reconstruction by use of first ten local energy containing modes provides an energy content of 73%; **c** original vortex no. V

to the original snapshot (Fig. 18c). Hereby, the *local* prime modes might not be identical to the first POD-modes. Obviously only structures with typical single vortex shape have as *local* prime modes the first POD-modes. In comparison, especially the pattern III (ref. Fig. 15a) consists of a double structure, and, consequently has as first modes the double structure eigenflow. Summation over the first 10 local modes allows an individual reconstructive quality for all 243 snapshots in the range from 48% up to 73%.

## 5 Stochastic estimation and its usefulness in the complementary technique

In this section we will present an application of the Linear Stochastic Estimation (LSE) (Adrian 1975) to the mixing layer data base. We will then focus on a complementary technique which employs the LSE method to extract phase information from application of the Proper Orthogonal Decomposition (POD) (Lumley 1967) to the same mixing layer.

Stochastic estimation uses the conditional information specified about the flow at one or more locations in conjunction with its statistical properties (the two-point correlation tensor) to estimate the information at the remaining locations. Here the thrust will be to utilize the instantaneous velocity at select  $y$  locations in the mixing layer to estimate the instantaneous velocity for all  $y$  locations. For the mixing layer data base, the instantaneous velocity is available at all  $y$  locations (where there are probes). In many other experiments, this is not the case due to a lack of a sufficient number of channels of hot-wire anemometry data acquisition and A/D conversion. Hence, it is advantageous to use the rake data base since it allows us to check the validity of the approach by comparison between estimated and measured time series. Note that a minimum of two probes and associated hardware are necessary to apply the following ideas to any experiment because of the need for the *two-point* statistics.

Adrian (1975) studied conditional flow structures in isotropic turbulence by computing estimates of the velocity  $u(y+r, t)$  given that the velocity at  $(y, t)$  assume some specified value  $u(y, t)$ . It was found that this simple flow, when sampled in a statistical sense, shows the existence of organized structures. Tung and Adrian (1980) studied the influence of the second, third and fourth order terms on the estimate. Their results indicated that the contribution from higher order terms to the overall estimate was insignificant, hence the use of the linear stochastic estimate in this study.

A one-dimensional (in  $y$ ) linear stochastic estimation yields an estimate

$$\tilde{u}_i(y', t) = A_{ij}(y') u_j(y, t) \quad (16)$$

with  $A_{ik}$  computed from

$$\overline{u_j(y) u_k(y') A_{ik}(y')} = \overline{u_j(y) u_i(y')} \quad (17)$$

where  $\overline{u_j(y) u_k(y')}$  and  $\overline{u_i(y) u_i(y')}$  are the Reynolds stress and two-point correlation tensors, respectively. It should be noted, for these systems of equations, only the two-point space (in  $y$ ) correlation data is utilized. These systems are not a function of the condition being investigated. For further discussion on the Stochastic Estimation theory see Adrian and Moin (1988), Cole et al. (1992) and Guezennec (1989).

As mentioned earlier, in this work we estimate the velocity components across the mixing layer from the expansion of Eq. (16) utilizing the actual velocity components at select positions in  $y$ . Here, it is not the intent to present a detailed discussion on what number of probes or their respective positions are the most appropriate to obtain the best estimate of the velocity field. These issues are discussed in Delville et al. (1993) for the present mixing layer data base and in Cole et al. (1992) for a jet mixing layer.

Figure 19a presents the vector plot of the *measured* velocity field. This replot of Fig. 5d is included here to ease comparison to the estimates. Figures 19b–d show various linear stochastic estimates of the vector field where the condition points are indicated by the arrows. Figure 19b presents a one-point estimate, whereas Fig. 19c and d present two-point estimates. For the two-point cases, the probes which supply the condition are equally spaced on either side of the centerline. Comparison of Fig. 19b–d with Fig. 19a indicates the quality of each respective estimate. It is clear that the estimate shown in Fig. 19d provides the best comparison. Note, in particular, how both the amplitude and phase of the velocity vector field are reasonably preserved with this estimate.

As a result of the above, the estimated time series shown in Fig. 19d will be used in conjunction with the POD to implement the complementary technique. This complementary technique consists of three main steps. First, the eigenvectors and eigenvalues are obtained from direct application of the POD to a two-point spectral tensor as discussed in Sect. 4 of this manuscript. Second, the LSE is applied to the cross correlation tensor, and multipoint estimates of the random vector field are computed as presented above for the mixing layer. Third, the eigenvectors obtained from step one are projected onto the estimated velocity field obtained from step two to obtain *estimated* random coefficients. These estimated random coefficients are then used in conjunction with the POD eigenvectors to reconstruct the estimated random velocity field.

Mathematically the stochastic estimates of the random coefficient are calculated from:

$$a_n^{est}(f) = \int \hat{u}_i^{est}(y, f) \psi_i^{(n)*}(y, f) dy \quad (18)$$

where in this case  $\hat{u}_i^{est}(y, f)$  is the two-point linear stochastic estimate of the velocity field and  $\psi_i^{(n)*}(y, f)$  is obtained from the original POD eigenvalue problem. The estimated stream-wise velocity can be reproduced in Fourier space by

$$\hat{u}_i^{est}(y, f) = \sum_{n=1}^{\infty} a_n^{est}(f) \psi_i^{(n)}(y, f) \quad (19)$$

and then inverse transformed to obtain  $\hat{u}_i^{est}(y, t)$ . For further details on this technique refer to Bonnet et al. (1994), Glauser et al. (1993) and Ukeiley et al. (1993).

Figure 20a shows the contribution from the first POD mode using the *measured* instantaneous velocity field, Fig. 19a, in the projection as presented in the previous section. The first POD mode retain most of the large scale features exhibited in the original field. The application of the complementary technique is shown in Fig. 20b. Here the eigenvectors, obtained from the direct application of the POD, are projected onto the estimated field using the estimated data presented in Fig. 19d.

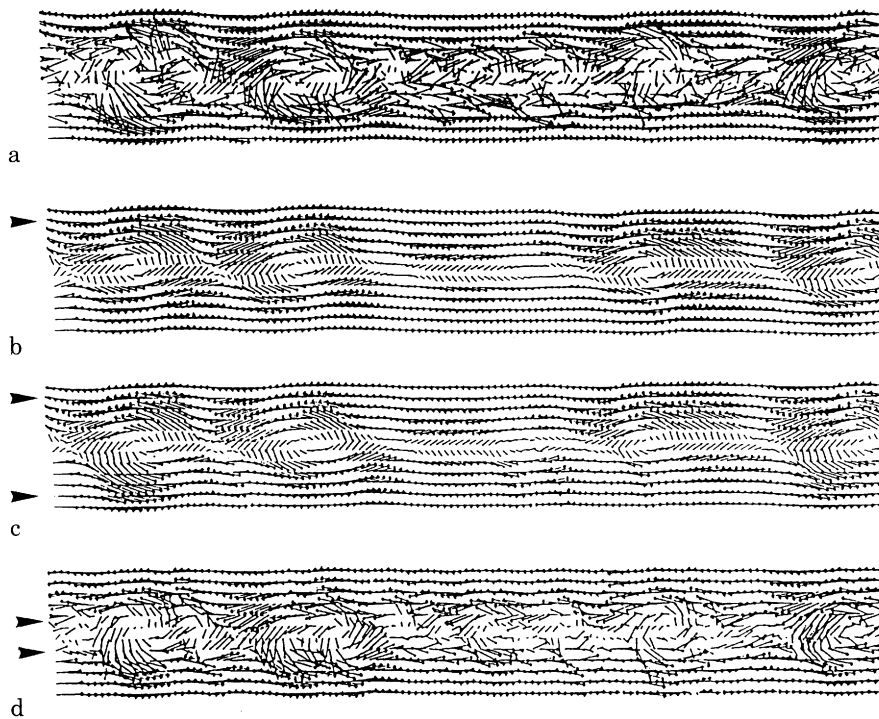


Fig. 19a–d. Examples of Linear Stochastic Estimation. For several conditions. **a** Original instantaneous velocity vector plot; **b** LSE with 1 condition; **c** and **d** with 2 conditions. The reference signals are indicated by the arrows on each example (same scale as for Fig. 5)

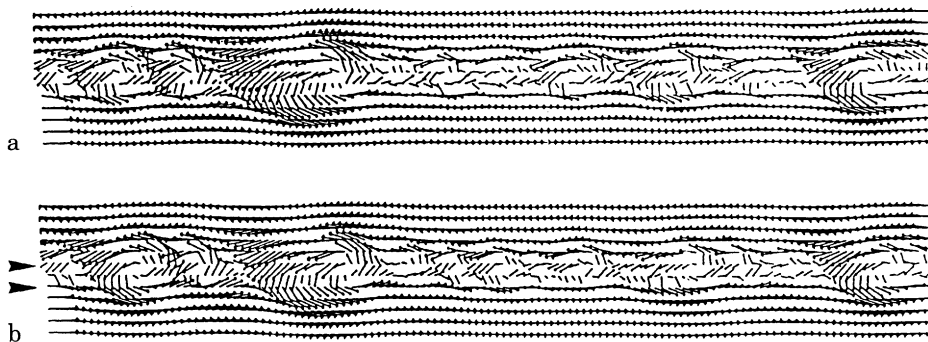


Fig. 20a, b. Complementary technique. **a** First POD mode from full measured field; **b** reconstructed using the stochastic estimated field (same scales as for Fig. 5)

Reasonable estimates of the large scale structure are obtained, even though only 17% of the *measured* instantaneous data has been used. In fact, one see that Fig. 20b compares quite well to Fig. 20a which was computed using the full *measured* instantaneous velocity field.

In order to quantitatively assess the technique, the streamwise root mean square (RMS) velocities are computed from the estimated and original velocity fields and comparisons are made, see Fig. 21. The percentage of the streamwise RMS velocity captured using the complementary technique is very close to that obtained from the direct application of the POD for the first mode. These results show that the complementary technique, which combines LSE and POD, allows one to obtain time dependent information from the POD while greatly reducing the amount of instantaneous data required. Hence, it may not be necessary to measure the instantaneous velocity field at all points in space *simultaneously* to obtain the phase of the structures, but only at a few select spatial position.

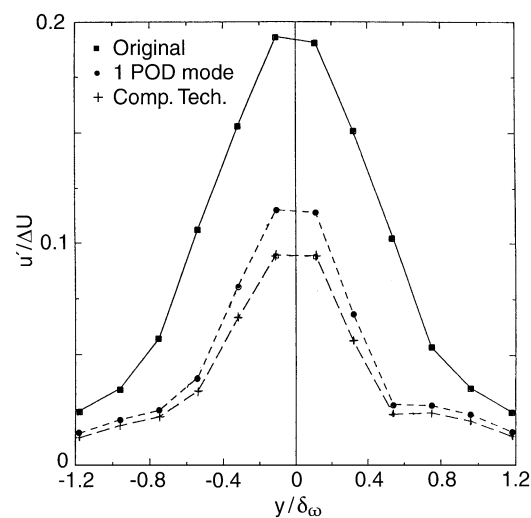


Fig. 21. RMS Comparisons

## 6

### Vorticity-based identification methods

#### 6.1

##### Overview of the method

Although the eduction approach in principle applies to the 3D vorticity field, limitation of experimental data to data forced us to use one vorticity component in a 2D plane, namely  $\omega_z$  in the  $x$ - $y$  plane. The eduction process strictly corresponds to the method introduced by Hussain and Hayakawa (1987) and used by several authors. In principle, it consists of the following steps: (i) choose smoothed spanwise vorticity as a feature that denotes passage of large-scale structures, (ii) select the most dominant structures based on their vorticity magnitude and size, (iii) phase align the accepted structures and obtain their ensemble average, (iv) refine the phase average by an iterative procedure that is based on the cross-correlation of individual realizations and their ensemble average (this step only rejects structures which are too far from the average), and (v) compute by ensemble averaging relevant coherent and incoherent quantities that are important to the dynamics of the flow from the *unsmoothed* data. Thus, smoothing, used only for identification of structures in the random vorticity field, does not affect any of the educed quantities: coherent or incoherent.

One advantage of such an eduction scheme is its potential use to study the dynamics of CS in any flow. This is possible through a conditionally averaged equation derived from the Navier–Stokes equation after decomposing the instantaneous field into coherent and incoherent parts (see Hussain 1983). Another advantage is that the educed incoherent quantities provide information about the dynamics of the small-scale motions.

In the present application of this method to the mixing layer data base, we intentionally made no attempts to improve or adapt the method as it can be considered “classical” since it has been applied extensively by several groups. Particularly, the rejection criteria used in step (iv) and the smoothing process introduced at the end of the eduction process (after step (v)) were the same than those originally introduced by Hussain and Hayakawa (1987) and used for several other flows applications (see for example Jeong et al. 1993). The use of this method in this context should therefore be considered as a comparative test case for less widely used conditional methods, such as the ones described in the next two sections. In addition, the results of the application of the vorticity-based method can be considered as a blind test since all the original components of the method have been implemented. This clearly will be born out when the efficiency of the method will be discussed in Sect. 9.

#### 6.2

##### Application of the method to the data base

Since vorticity cannot be directly measured from  $u$ ,  $v$  signals from hot wires, we have to depend on Taylor’s hypothesis to identify structures in the instantaneous flow field. For the convection velocity in Taylor’s hypothesis, we used the convection velocity  $U_c$ .

Since our primary interest is in large-scale events, the determination of the ensemble averages was performed on the

smoothed instantaneous spanwise vorticity data which were obtained by local spatial smoothing. In the present case, a nine point averaging ( $3 \times 3$  in an  $x$ - $y$  plane) was used; this operation smoothes out the fine-scale fluctuations but retains the underlying large-scale vorticity. Once again, note that all structure properties are finally educed from the unsmoothed data, then the smoothing process is not essential, as it has been shown in other comparable applications of the Hussain and Hayakawa’s eduction method (see for example Jeong et al. 1993).

The first condition employed by the present eduction scheme is for the structure strength. Based on that, realization (distributions in the streamwise-transverse plane) with maximum smoothed  $\omega_z$  exceeding  $2S_M$  (where  $S_M$  is the maximum mean shear) are detected at each spanwise plane. The choice of the local  $S_M$  for specifying the threshold is justified by the fact that both  $S_M$  and the structure strength evolve in  $x$ . The second condition is for the structure size. In order to specify this,  $\omega_z$  is required to be higher than  $0.3S_M$  within distance of  $0.25d$  (here  $d$  is the size of spanwise structure, which was obtained from the structure boundary of the ensemble averaged vorticity after the first condition was applied) from its peak in the  $x$ - $y$  plane.

Each realization is then aligned with respect to the peak of  $\omega_z$  and averaged to obtain the zeroth-order ensemble average. Each realization is then shifted in both the  $x$  and  $y$  directions to maximize its cross-correlation with the zeroth-order ensemble average in order to obtain sharper structure boundaries. This process is iterated until convergence in structure shape is achieved. The purpose of the iteration is to find the underlying, true center of each realization necessary for its optimal alignment before its inclusion in the ensemble average. Note that the location of maximum spanwise vorticity can only give a local peak and not the center of the overall structure, which can be obtained from the location of maximum cross-correlation in this study. Realizations that produce a weak cross-correlation coefficient, here below 0.8, or require shifts of more than  $0.5d$ , were discarded because they are significantly different from the ensemble-averaged structure. Note that this iteration process is similar to the pattern recognition technique, provided that the zeroth iteration ensemble-average is considered as the trial pattern. Here, the trial pattern is not guessed but derived from the signals themselves. After a new alignment of the realizations through the modified peak locations, the smoothed data are discarded and only the unsmoothed data are used to obtain the final ensemble average. Whatever survives the ensemble average is the coherent structure; the departure of each accepted realization from the average is the incoherent turbulence in that realization. Incoherent turbulence is then rms ensemble averaged to extract its statistical measures over the structure cross-section. The final ensemble averages were obtained after initially accepting about 1000 realizations and discarding about 200 realizations during the iteration.

Coherent vertical velocity (normal to the mixing layer plane,  $v$  Fig. 22a) and vorticity distributions (Fig. 22b) show that spanwise structures are the dominant features of this flow. Coherent vorticity contains a significant value even outside the spanwise structure unlike those in numerically simulated mixing layers (see Metcalfe et al. 1987). This is because this

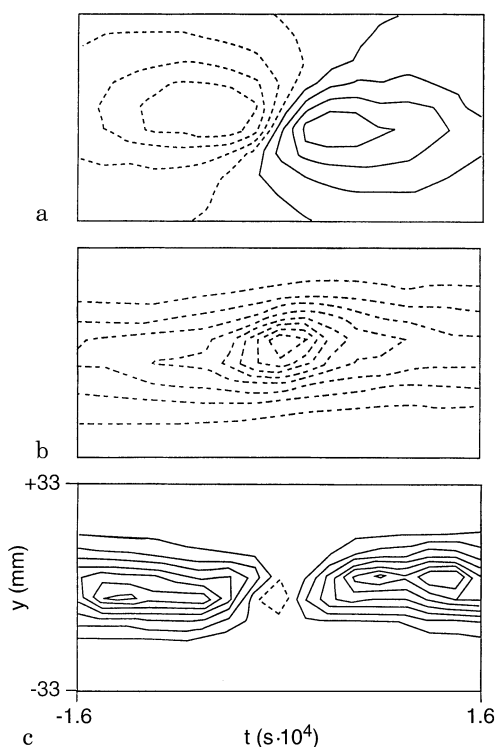


Fig. 22a–c. Ensemble average of the vorticity based conditional sampling. a Isocontour of  $\langle v \rangle$ ; b isocontours of  $\langle \omega_z \rangle$ ; c isocontours of  $P_t$

flow is initially turbulent, and the shear layer is initially diffused. From these results, several quantities can be calculated, such as  $\langle u - U \rangle \langle v \rangle$  and turbulence production:

$$P_t = - \left\langle \frac{\partial u}{\partial y} + \frac{\partial v}{\partial x} \right\rangle \langle u, v_r \rangle - \left\langle \frac{\partial u}{\partial x} \right\rangle \langle u_r^2 \rangle - \left\langle \frac{\partial v}{\partial y} \right\rangle \langle v_r^2 \rangle$$

where the subscript  $r$  stands for the random part of the signal.  $P_t$  indicates production of incoherent turbulence by coherent motion, i.e. the stretching of ribs by adjacent rolls.

It is known from the literature that, in plane turbulent mixing layers, the intermediate-scale structures such as ribs are oriented in the streamwise direction, and hence cannot be seen in the present ensemble averages of velocity and vorticity. This scenario is consistent with the spatial distribution of the coherent production  $P_t$  plotted in Fig. 22c). This corresponds to the dominance of ribs away from the structure between two successive spanwise structures, implying that ribs occur, even in this initially turbulent flow, due to vortex stretching by successive structures and are still dynamically dominant.

## 7

### WAG, filtering and vorticity peaks methods

Several complementary methods to investigate the structure of turbulent shear flows have been developed at the University of Newcastle. Generally, they are applied in a three-stage process. Firstly, the available data from a particular flow are examined (with as little bias as possible) for evidence of organized structure. The second stage is to apply the most appropriate methods to detect and analyze the identified type(s) of

structure. The final (and ultimately most important) stage is to determine the extent to which, and in what manner, the organized structure(s) contribute to flow dynamics. The particular detection methods such as WAG or peak vorticity are regarded as subservient to the main process of flow analysis. In this section, the three-stage approach is applied to the low sampling frequency samples of the database. Stage one (examination of data) includes: (i) direct inspection of continuous data records by means of sectional streamlines, contour plots of velocity fluctuations, contours of instantaneous spanwise vorticity  $\omega_z$ , etc., and (ii) conventional Fourier transform power- and cross-spectra, contours of auto- and cross-correlations, and so on. Stage two comprises: (i) detection of structures that have intense, fairly small-scale concentrations of  $\omega_z$ ; (ii) WAG-detection (Window Average Gradient) of larger scale structures in terms of their characteristic signatures in  $u$  and  $v$  signals; (iii) probability analysis of the time delays between detection instants; (iv) selection of detection subsets based on specified time delays, equivalent to a high-Q (very selective) band-pass filtering process in the time domain; and (v) conventional conditional averaging based on detection sets of selected subsets. The main purpose of subset selection (filtering) is to reduce smearing of conditional averages. Stage three involves a study of the proportions of momentum transfer ( $\overline{uv}$ ) and turbulent energy ( $u^2$  and  $v^2$ ) that are contributed by the organized structures.

## 7.1

### Stage 1

Fourier analysis of the mixing layer gives a strong indication of dominant structures with a period of about 2.7 ms. However, cross-spectral and cross-correlations imply that the effects of these structures are rather different in the middle or at the edges of the mixing layer. For the middle six probes, cross-spectra are negative at all frequencies, and the correlation coefficient  $R_{uv}$  peaks at about  $-0.4$  at zero time delay. For the outer probes, cross spectra have very low magnitude while  $R_{uv}$  is alternately positive and negative with high magnitude ( $>0.6$ ) at  $\pm 0.7$  ms time delay. Thus the middle part of the flow is typical of fully turbulent shear flow, while the upper and lower edges behave like irrotational flow around a series of structures between them.

Simultaneous records of  $(u, v)$  from the 12 X-probes allow plenty of scope for study of instantaneous flow structure. Some samples of sectional streamlines and contours of spanwise vorticity  $\omega_z$  are shown in Fig. 23. Sectional streamlines, which are lines parallel to the measured two-dimensional velocity vectors, are not true streamlines because they assume that the flow is steady and two-dimensional, but they seem to be better suited to the human eye than ordinary vector plots as a form of pseudo-visualization. The sectional streamlines of Fig. 23 give a very strong impression that a mixing layer is dominated by spanwise vortex-like structures. Their longitudinal scale is quite variable, but the structure at  $x = 100$  mm in Fig. 23c is most typical, and corresponds to the scale inferred from Fourier analysis. The larger structure at the middle of Fig. 23a could well be composed of two smaller structures that are in the process of pairing, as discussed later.

Contours of  $\omega_z$  in Fig. 23b and d imply that vorticity is concentrated into regions that are actually much smaller than

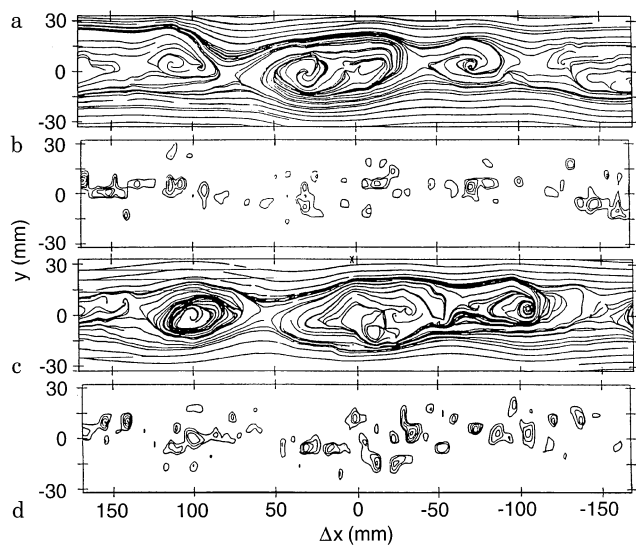


Fig. 23a–d. Two patches of instantaneous data: a, c sectional streamlines and b, d spanwise vorticity  $\omega_z$ . Contours ( $s^{-1}$ ):  $-1000$ ,  $-1500$ ,  $-2000$ , ...

the dominant vortex-like structures. Smaller scales are to be expected for longitudinal braid vortices, but they have mainly  $\omega_x$  and  $\omega_y$  components. It is possible that  $\omega_z$  on this scale is associated not only with braid vortices but also with the dominant spanwise structures from further upstream where all scales are smaller, and which are merging and being stretched and distorted at the present measurement station.

## 7.2

### Stage 2

Detection of locations of  $\omega_z$  negative peaks was based on the approximation  $\omega_z \approx \Delta v/\Delta x - \Delta u/\Delta y$ , where  $\Delta x = -U_c \Delta t$  and  $\Delta t = 0.2$  ms (two sampling intervals) making  $\Delta x \approx 6.8$  mm, and  $\Delta y = 6$  mm, the spacing between adjacent probes. (Note that  $\Delta t = 0.1$  ms for  $\omega_z$  contours in Figs. 23, 25 and 26). Each detection point is the position of most negative  $\omega_z$  within each patch of data for which  $\omega_z$  is continuously less than  $-1000$   $s^{-1}$  (same for all  $y$  positions). The present small-scale vorticity approach is much simpler than that used by Hussain and co-workers (e.g. Hussain and Hayakawa 1987) for large-scale detections inasmuch as there is no need to smooth the velocity or vorticity data over the much larger area of a large scale structure, and there is no need for an iteration process either. For pairs of probes near the edges of the mixing layer there were very few detections, but the detection frequency around the middle was 700–900 Hz, at least double the frequency of dominant large scale structures and consistent with Fig. 23b and d.

Velocity components from all probes were conditioned on a set of 900  $\omega_z$  detections from the probes nearest to the centreline and the corresponding sectional streamlines and contours of  $\omega_z$  are shown in Fig. 26a and b. It is clear that this is fairly small structure without a well-defined period. The level of  $\omega_z$  is quite strong, however, being almost  $-1500$   $s^{-1}$  at the center.

Detection of the dominant large scale structures was carried out with the single-point WAG method, described in Bisset

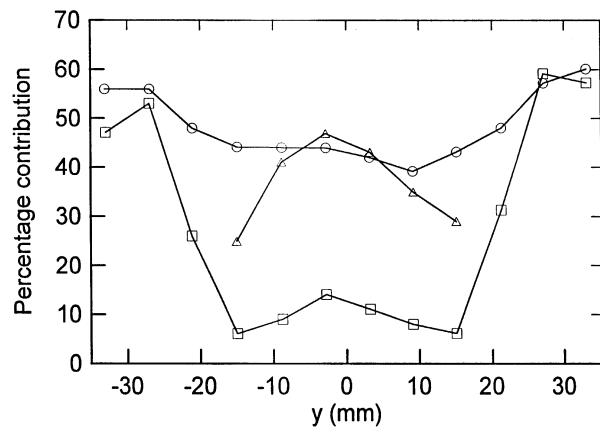


Fig. 24. Percentage contributions to  $\overline{u^2}$  (□),  $\overline{v^2}$  (○) and  $\overline{uv}$  (△) made by large scale structures (WAG  $v$  detections)

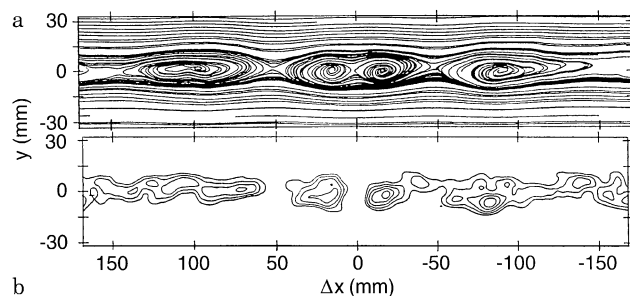


Fig. 25a, b. Conditional averages of structures possibly undergoing pairing. a Sectional streamlines and b  $\omega_z$ . Contours ( $s^{-1}$ ):  $-500$ ,  $-600$ ,  $-700$ , ...

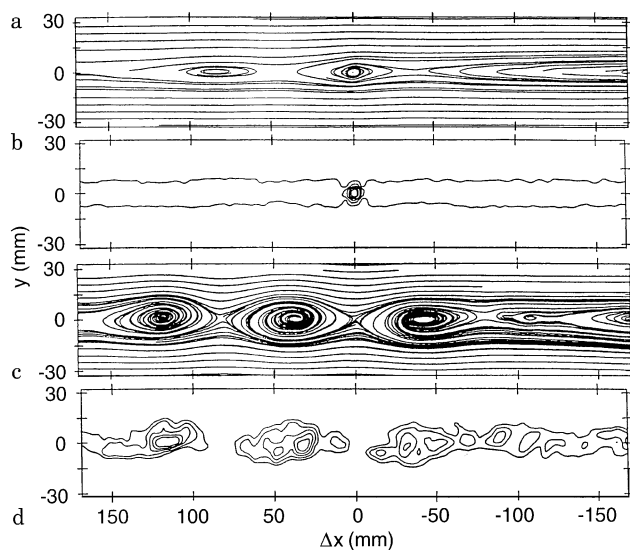


Fig. 26a–d. Conditional averaging of small and large scale structures. a sectional streamlines and b contours of  $\omega_z$  based on vorticity detections at  $y=0$ ; c sectional streamlines and d contours of  $\omega_z$  based on pair of WAG  $v$  detections at  $y=-3$  mm separated by 2.4 ms. Contours ( $s^{-1}$ ):  $-500$ ,  $-600$ ,  $-700$ , ...

et al. (1990). WAG was designed as a more effective replacement for VITA (e.g. Blackwelder and Kaplan 1976). The essence of the method is to move a window through the data, and find the difference between the average data value in the

second half of the window and the average in the first half. Local maxima in this difference of correct sign and sufficient magnitude are accepted as detection points. Window length controls the scale of structure that can be detected.

Although WAG is capable of detecting structure centers, it is generally used to detect the rather sharper  $u$  or  $v$  gradients that occur in the vicinity of saddle points between structures, or (in the case of wall-bounded flows) in connection with  $\delta$ -scale discontinuities or near-wall shear layers. Previous practice was followed here, and independent sets of detections were obtained for positive jumps in  $u$  and negative jumps in  $v$  from all X-probes. The detection window length was 1.9 ms (optimum for events of period 2.7 ms), and the threshold was 0.4 (normalised by the rms value). The resulting detection frequency was a little over 300 Hz independent of  $y$ , except slightly lower for  $u$  detections in the central region. Initially, velocities from all probes were conditioned on several separate detection sets from different probes. The corresponding sectional streamlines, which all show large vortex-like structures on both sides of the detection point, were given in Bonnet et al. (1993). The detection point itself appears as a saddle point.

Relationships between different sets of detections (including  $\omega_z$  detections) were explored through time delay analysis. Firstly, the probabilities of given time delays between successive WAG  $v$  detections (from the same set) were obtained; the probability was maximum at  $\Delta t = 2.4$  ms in nearly all cases. Figure 26c and d show sectional streamlines and contours of  $\omega_z$  based on a subset of  $v$  detections from the probe at  $y = -3$  mm that were selected only if the previous detection occurred  $2.4 \pm 0.1$  ms earlier (about 18% of all detections). This selective filtering process reduced smearing of the second of the three structures shown and ensures that it has the most typical length. The level of  $\omega_z$  is lowest in the vicinity of saddle points between structures, but it is not especially strong anywhere. Time delay analysis also shows that: (i) WAG  $v$  detections tend to occur simultaneously on all probes; (ii) WAG  $u$  detections are fairly close to WAG  $v$  detections in the central region, but on the high speed side WAG  $u$  detections lag  $v$  by about 0.6 ms, and on the low speed side  $u$  detections lead  $v$  by about 0.7 ms (consistent with results for  $R_{uv}$ ); (iii)  $\omega_z$  detections are not strongly correlated with the larger WAG detected structures, but they have some tendency to collect in the middle of the larger structures and avoid the saddle regions; (iv) WAG  $u$  detections from the four probes nearest to the centreplane tend to fall along a line at about  $40^\circ$  to the  $x$ -axis, i.e. there is a type of longitudinal velocity interface here; and (v) there is no distinct relationship between  $u$  detections in the central and outer regions, unlike  $v$ .

### 7.3

#### Stage 3

Up to this point, the results mainly concern flow kinematics, but it is important to try to quantify the contributions that the detected structures make to flow dynamics. In this case the contributions to turbulent energy and momentum transfer were determined. The quantities  $\langle u \rangle^2$ ,  $\langle u^2 \rangle$ ,  $\langle v \rangle^2$ ,  $\langle v^2 \rangle$ ,  $\langle u \rangle$ ,  $\langle v \rangle$  and  $\langle uv \rangle$  (where angle brackets denote the usual conditional averaging procedure) were calculated for  $\pm 1.2$  ms

relative to WAG detection points (i.e.  $\pm$  half a typical structure length) and then averaged over that length. Around 80% of all data points were used in forming the averages; and, therefore,  $\overline{\langle u^2 \rangle} \approx \overline{u^2}$ ,  $\overline{\langle v^2 \rangle} \approx \overline{v^2}$  and  $\overline{\langle uv \rangle} \approx \overline{uv}$  (where the double overbar indicates the structure-length average). The ratio of  $\overline{\langle u \rangle}$  to  $\overline{\langle u^2 \rangle}$  (or  $\overline{u^2}$ ) indicates the contribution that the detected structure makes to the  $u$  component of turbulent energy, and similarly for  $\overline{v^2}$ . The ratio of  $\overline{\langle u \rangle \langle v \rangle}$  to  $\overline{uv}$  quantifies the contribution of the structures to momentum transfer across the mixing layer. These ratios are plotted for WAG  $v$  detections from all  $y$  positions in Fig. 24, except that the contribution to  $\overline{uv}$  the outer regions tends to be zero divided by zero and is therefore omitted. The contributions to  $\overline{v^2}$  and  $\overline{uv}$  in the central fully turbulent zone are quite substantial at more than 40%; whereas the contribution to  $\overline{u^2}$  is around 10%. When detection is based on  $u$ , the contribution percentages to  $\overline{u^2}$  and  $\overline{v^2}$  are more-or-less reversed; but the percentage for  $\overline{uv}$  changes little. The values here are similar or slightly higher than those found for a plane far-wake (Antonia et al. 1987); values for boundary layers (Antonia et al. 1990) are generally somewhat lower (except perhaps at low  $R_\theta$ ). Results near the edges of the mixing layer are unusual, not only for the large percentage contributions but also because the values for both detection and non-detection signals are similar. It is much more difficult to estimate the contributions from the smaller  $\omega_z$  detected structures because there is no probe passing through the structure centre, but initial estimates put the contributions at about 10% for  $\overline{v^2}$  and  $\overline{uv}$ , and even less for  $\overline{u^2}$ .

### 7.4

#### Selective filtering to show pairing

Given that pairing of structures is an important aspect of the downstream development of mixing layers (e.g. Winant and Browand 1974), it seemed worthwhile to follow up the inference that instantaneous data show structures in the process of merging (e.g., Fig. 23a). Unlike the results above, which show the predominant structure in its most typical conditionally averaged form, the results that follow are intended to show the versatility and selectivity of WAG and selective filtering. Assuming that the structures undergoing pairing are smaller than the “standard” large scale structures, a new set of WAG  $v$  detections was obtained with the averaging window reduced to 0.9 ms. Many of these were the same as the “standard” detections, but some fell in between. A small subset was selected on three criteria: (i) no “standard” WAG  $v$  detection within  $\pm 0.2$  ms; (ii) a “standard” detection present at  $-1.4 \pm 0.5$  ms; and (iii) a “standard” detection at  $1.4 \pm 0.5$  ms. About  $5\frac{1}{2}\%$  of the original small-scale detections satisfied all three criteria, including one at  $x = 10$  mm in Fig. 23a. Figure 25 shows sectional streamlines and  $\omega_z$  contours corresponding to the selected detections. The appearance of two smaller structures bound up in a larger structure seems quite convincing, but with one fixed set of probes it is not possible to study the actual process of pairing through all stages. It should also be noted that many pairs of structures would be offset in the  $y$  direction instead of  $x$  as they pass the probes and would, therefore, not be captured by the present type of detection/filtering process.

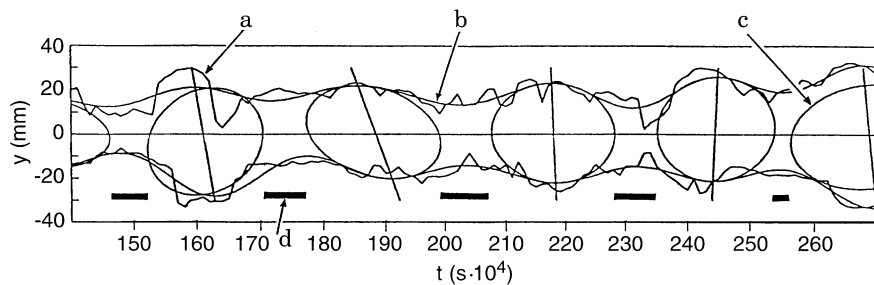


Fig. 27. Schematic description of the Delocalized Conditional Sampling Method. *a* Raw frontier; *b* smoothed frontier; *c* fitted ellipses; *d*  $I=1$  time stamps

## 8 Delocalized conditional sampling method

### 8.1 Description of the method

Conditional sampling based on one or two point measurements has been extensively used in free shear flows by several authors, see for example Browand and Weidman (1976), Antonia (1981), Zaman and Hussain (1984). When the information is available from a rake of sensors simultaneously in several locations in space, it is possible to automatically select the two optimal probes that will serve for the detection. With this technique each probe plays a role in the detection procedure and is used to compute the ensemble averages. The advantage of this method lies in its ability to detect structures of any size appearing at any transverse position and with any phase shift inside the structure.

The DCS algorithm follows a two-step procedure. The first step determines a “pre-partitioning” of the flow which allows the time of observation to be split into two parts, corresponding respectively to the instants when CS are present and when they are not. The second step identifies the location of the CS within the pre-determined time periods. The corresponding statistics of these events can then be built as usual. The following sections described the two steps of the detection procedure.

#### 8.1.1 First step: pre-partitioning

The simplest and, in some sense, the least ambiguous approach to select the different phases of the flow is to examine the instantaneous velocity field. This is performed according to the procedure illustrated in Fig. 27. First of all, low and high threshold values are applied to the longitudinal ( $u$ ) velocity signal. The instantaneous, external “boundaries” of the flow are then determined for both the low and high speed sides of the mixing layer. These boundaries are then smoothed: a low pass frequency filtering is applied, where the cut-off frequency is of the order  $1.25 f_p$  and  $f_p$  is the Strouhal frequency (see Fig. 7b). It has been demonstrated that the extracted edges remain basically unchanged for a cut-off frequency varying in the range  $f_c/f_p \sim 1-2$ , see Bellin (1991). A correspondence between the two sides of the boundaries is established by fitting ellipses which link the closest local extrema. These ellipses are chosen automatically, by using a least square procedure, to fit both edges over a time duration of the order of  $T_p/8$ . Some

additional checks are performed in order to retain only relevant events (e.g., the  $y$  extent of the ellipses has to be greater than  $\delta_w$ , the ellipses must not overlap, etc). These checks have been selected by analyzing probability distributions of characteristic parameters.

The choice of ellipses is, at this stage, arbitrary; but this choice is only a secondary importance because the ellipses are only used to build a pre-detection function. We will demonstrate later on that, for the present configuration, this function is 0 when CS are present. The conditional sampling itself can then be applied during these periods of better efficiency. This pre-partitioning procedure is rather insensitive to the threshold selected for the partition. Bellin et al. (1993) show that a significant variation of this threshold (from 4 to 10% of the external velocities) does not strongly modify the puff edges locations and, therefore, the detector function  $I(t)$ . More precisely, the main consequence of a threshold level which is too low is only to miss some  $I=1$  events. Hence the time period of the application of the DCS is increased without any benefit.

Conventional ensemble averages can be directly obtained from this detector function as well. Figure 28 shows the iso-contours of the vorticity obtained when the reference time is centered on  $I=0$  (Fig. 28a) or on  $I=1$  (Fig. 28b). From the topology of the iso-contours, it clearly appears that the results obtained when  $I=0$  correspond to the presence of Coherent Structures. The criterion  $I=0$  can be associated, therefore, with the probable presence of CS, justifying the above-mentioned criterion.

#### 8.1.2 Second step: DCS

The conditional procedure itself can be applied during the pre-determined periods of time that correspond to high probable occurrence of CS selected from the first step ( $I=0$ ).

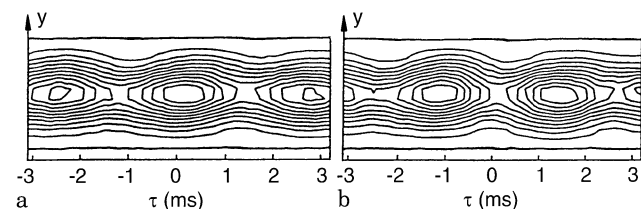


Fig. 28. Ensemble averages centered on  $I=0$  time stamps *a* and  $I=1$  *b*

During each selected period, the algorithm selects the location  $(Y_1, t_1)$  where the fluctuating velocity (longitudinal component) reaches its maximum value on the high speed side. It also determines the  $(Y_2, t_2)$  location of minimum value on the low speed side. According to the conventional concept of coherent structure in plane mixing layers, these two locations correspond to the upper and lower edges of the CS. This procedure is equivalent to automatically selecting optimal detector placements from the available measurements locations instead of *a priori* positioning which is the case for conventional detector use. The DCS results in lower rejection rates than conventional techniques and allows new statistics for several characteristics of the CS to be computed. Indeed,  $|Y_1 + Y_2|/2$  represents an estimation of the location of the CS center. In addition, the time shift between the two detections,  $t_1 - t_2$ , contains information on the stage of the evolution of the CS. This can be related to the different phases of the life of the structures as will be illustrated later. It is then possible to build *conditional* ensemble averages taking into account three independent parameters or CS characteristics: the thickness, center location (relative to the mixing layer axis), and phase shift (between the two opposite sides of the CS).

## 8.2

### Typical results

The method has been applied to the database. The typical detection times obtained for the reference sample are given in Sect. 9 (Fig. 32). Clearly each detection time visually corresponds to each large scale event. Figure 29 shows typical statistics that can be obtained from the data base. In this case, the joint probability density of thickness and phase can be computed. For the present data base, the most probable value of the thickness is  $1.12\delta_w$  and the most probable phase is zero degrees.

It is also possible to analyze the time interval between two successive structures. By implementing Taylor's hypothesis, the most probable distance between structures is evaluated to be of the order of  $3\delta_w$ . This value is in agreement with the results of other authors in comparable configurations (Bernal 1988). A more detailed analysis of the statistics that can be derived from this DCS can be found in Bellin et al. (1993).

With this method, it is possible to select a given class of size, position, and phase shift and then build the corresponding conditional averages. Figure 30 illustrates the influence of the time shifts on the resulting ensemble average of the structures detected. The sectional streamlines, after Bisset et al. (1990) are plotted on the figure. Zero time shift (Fig. 30a) corresponds to centered, one-core CS while, with no zero phase ( $-20^\circ$ , Fig. 30b), two cores can be observed, in particular on the vector plot. This last case corresponds to a period of pre-pairing processes, for example. Intermediate time shifts (not given here) show the successive stages of the evolution. The time shift between the two detection times  $t_1$  and  $t_2$  is translated in terms of phase according to the relation:

$$\Phi_d = \arctan(U_c \times (t_2 - t_1) / (y_2 - y_1)).$$

Some scatter can be observed when large time shifts are imposed, but this scatter never surpasses the observable shape of the CS. This procedure can be systematically used for

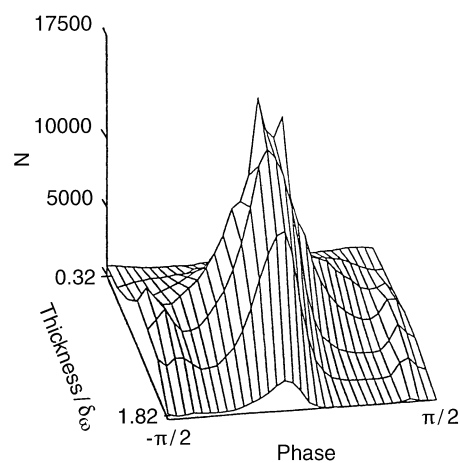


Fig. 29. Joint PDF of thickness-phase from DCS.  $N$  = number of events

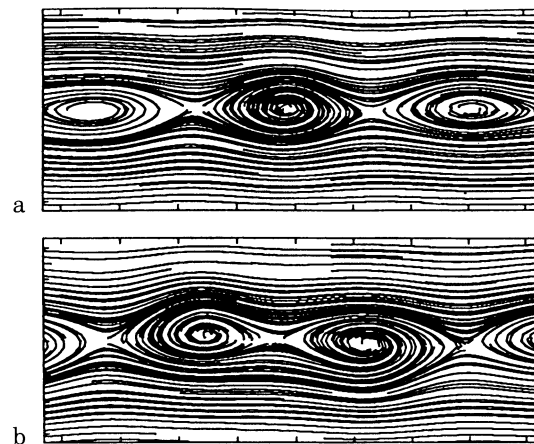


Fig. 30a, b. Ensemble average from DCS. Sectional streamlines. a Average pattern, all events cumulated; b average structure with a phase shift corresponding to a pairing stage (same scales as for Fig. 28)

any available turbulent quantity. Moreover, marginal statistics can be more convenient for the analysis of these characteristics.

## 8.3

### Triple decomposition

As with any conditional sampling, a double or triple decomposition can be applied as introduced by Reynolds and Hussain (1972). The efficiency of the DCS process and the capability to select different characteristics of the CS (size and/or shift, ...) permits a more detailed analysis than normal techniques. Details on the results obtained from the data base can be found in Bellin (1991). A particular illustration is given in Fig. 31 which shows the iso contours of the production term  $-\langle u_r v_r \rangle \langle \partial u / \partial y + \partial v / \partial x \rangle$ . In the same manner as that used previously to analyze the influence of the phase shift on the ensemble average of velocity and vorticity, we can analyze the behavior of the production term during the different stages of the CS evolution.

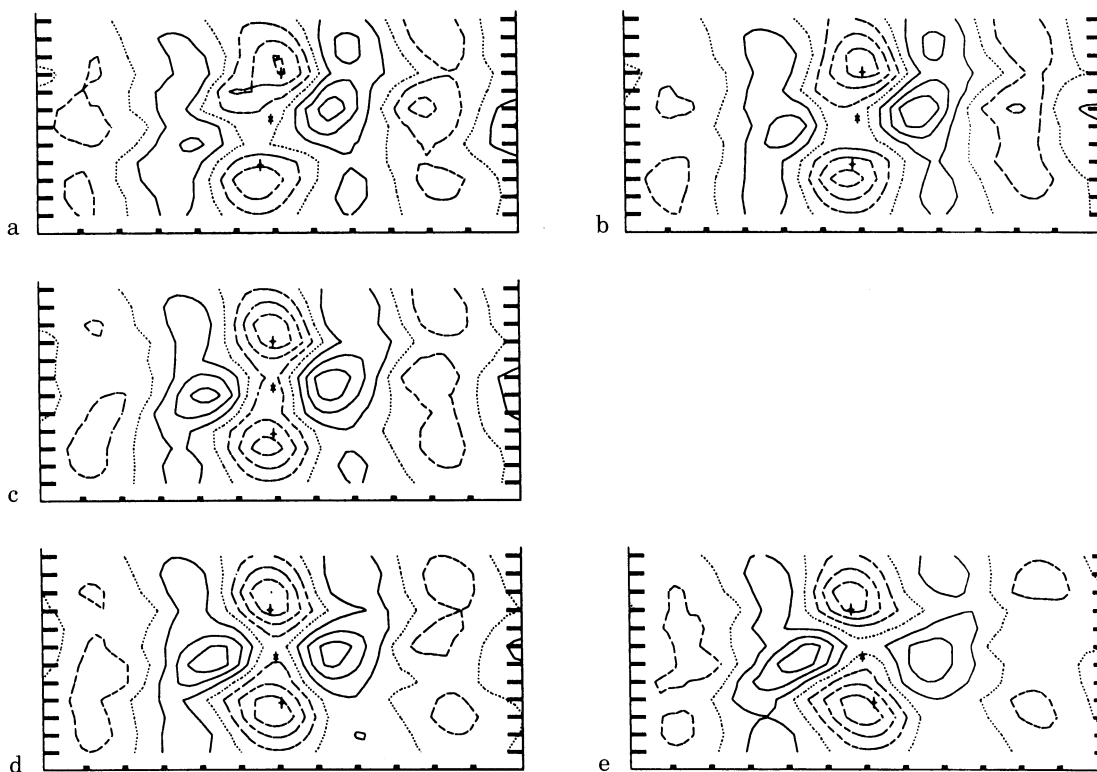


Fig. 31a–e. Influence of the phase shift on the coherent production:  $-\langle u, v, \rangle \langle \partial u / \partial y + \partial v / \partial x \rangle$  Phase shifts. a  $-14^\circ$ ; b  $-7^\circ$ ; c  $0^\circ$ ; d  $+7^\circ$ ; e  $+14^\circ$ . (same scale as for Fig. 28)

Figure 31 shows that influence of the phase shift, as expected, is not symmetrical. Positive phase shifts correspond to a greater self-induced rotation of positive and negative coherent production when compared to the effects of negative phase shifts. These effects closely correspond to a simple description of an isolated coherent eddy.

It should be noted that the iso-contours presented in the Fig. 31 are obtained by considering all the detected events regardless of their size or time shift. For the present results, 11,000 events have been used for the averaging process. The statistics can then be considered to be quite significant and reliable.

## 9

### Concluding remarks

In the previous sections, the results obtained from each method were presented. Some of these results can be considered to be unique to each method and, hence, cannot be directly compared. Such is the case for the spectra calculated from wavelets analysis, from direct time series, or from POD analysis, as well as for different statistics. However, these results can be used in a complementary fashion to characterize the flow. In contrast, several results obtained from the different methods have common features that can be used to identify similarities as well as differences between the different tests, and as much can be used to give reasonable information on the origin of discrepancies and similarities between the techniques. For these purposes, two types of comparisons will be made. First, the instantaneous information that is obtained

from the different methods will be compared and examples for the same time samples will be presented. The purpose of this step is to directly compare the local characteristics that can be obtained from each method: localization of the detection, visual representation associated, for example, with the mode decomposition via the POD, conditional instantaneous characteristics, etc. As a second step, conditional statistics will be used for more quantitative comparisons.

## 9.1

### Instantaneous information

#### 9.1.1

#### Instantaneous information from conditional sampling

The results of the application of the different detection criteria are presented in Fig. 32. The arrows indicate the detection times associated with the eddies in the mixing layer for the various techniques.

The velocity-based detection methods (wavelets, DCS, Correlation, WAG) result in detection times which are not too different from one another and exhibit frequencies which are consistent with the measured spectra. The wavelet detection of structures based on the branching of the wavelet transform obtained at  $y = -3$  mm, (arrows presented in Fig. 32a) is generally in good agreement with the visual inspection of the instantaneous vector plot although some differences are evident. The location of cones in the modulus of the wavelet transform may be used to detect vortical structure in the flow, and spatial statistics of the wavelet transform can give

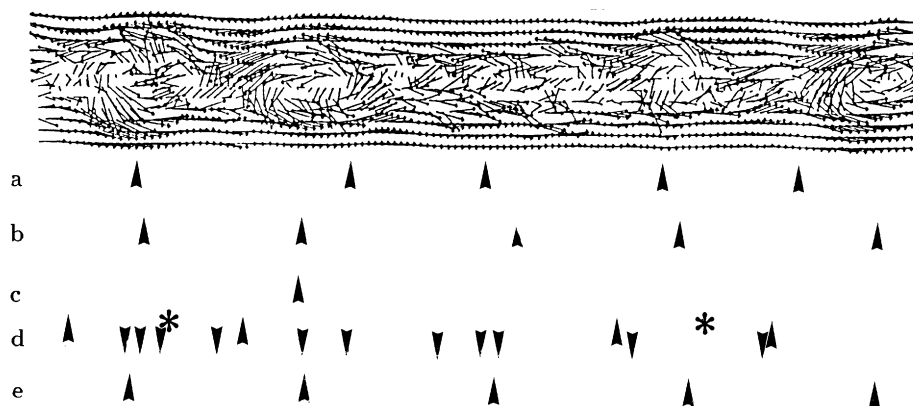


Fig. 32. Comparison of detection point from different methods. *a* Wavelets (Sect. 3); *b* correlation (Sect. 4.3); *c* vorticity-based detection (Sect. 6); *d* WAG method;  $\uparrow$ : detection based on  $v'$  at  $y = -3$  mm;  $\downarrow$ : detection based on  $w_z$  at  $y = 0$ ; \* pairing (Sect. 7); *e* delocalized detection (Sect. 8) (same scale as for Fig. 5)

information about how energy is distributed as a function of physical location and length scale. It is found that strong cones in the modulus of the wavelet transform, as the length scales  $a$  tend towards 0, point to the location of eddies and that the spatial fluctuation of wavelet energy increases with wavenumber and decreases towards the axis of the mixing layer.

The Delocalized Conditional Sampling and Correlation based detections are shown in Fig. 32e and b respectively. Both of these methods show excellent agreement with the visual inspection of the instantaneous vector plot. This is perhaps somewhat surprising since the DCS is a global technique while the correlation-based scheme is local in nature. Typical  $v$ -based WAG technique results are presented in Fig. 32d. The  $v$ -based WAG detections show the saddle points or interstructure occurrences and not the center of the structures, hence the difference in phase when compared to the other three velocity based techniques. Note that the WAG scheme misses the saddle point between 100 and 50 mm.

The results obtained from the application of the two different Vorticity-based Conditional Sampling schemes are shown in Fig. 32c (Houston group) and Fig. 32d (Newcastle group). As seen from Fig. 32c, only one structure is detected in this 0.0128 s sample. This results in a frequency of detection consistent with what was obtained when the entire data base was utilized (80 detections/10240 ensembles) as discussed in Sect. 6. The vorticity-based method from the Newcastle group, on the other hand, results in many detections (around 12) for this same sample as can be seen upon examination of Fig. 32e. This frequency of detection (940 Hz) is close to the band of frequencies of 700–900 Hz found when the one-second time records were utilized as discussed in Sect. 7. These significant differences between the two vorticity-based schemes are related to the differences in their makeup. The application of the Houston scheme is much more involved than that of the Newcastle group. The Houston scheme requires smoothing the velocity and vorticity data over a large spatial window as well as an iteration process. In addition, the Newcastle scheme is based solely on levels of vorticity whereas the Houston scheme requires an additional constraint related to the spatial scale of the structure.

Note that all the methods at least partially detect the second (from left to right) structure. This structure corresponds to the

maximum of  $\omega_z$  at  $x \simeq 100$  mm as shown in Fig. 4e. Also note, as mentioned above, that the WAG detection based on  $v$  catches the saddle point between  $x = 150$  and 100 mm but not between 100 and 50 mm. Hence the WAG method misses one side of the structure. The last structure on the right part of the time series is not properly detected by all of the methods. In this case the WAG method does detect the “roller” in the sense that the  $v$ -detection identifies the saddle point to its left and will also detect the saddle point to its right (not in the figure) if it is well defined. Also note, however, that the Newcastle  $\omega_z$ -based scheme roughly detects both of these structures. Hence, by comparing these two examples, we can conjecture that a combination of the WAG detection scheme and the simpler Newcastle vorticity-based approach may prove (to be fruitful) to enhance structure eduction.

The influence of the reference location in the  $y$  direction can explain why the wavelet method misses the timing on the far right structure. In the application given here, the reference signal is located below the axis ( $y = -3$  mm) so that the far right structure is not captured properly. This would also explain the difference in phase between the other structures obtained from the wavelets when compared to the correlation and Delocalized detection schemes as shown in Fig. 32b and e, respectively.

For the vorticity-based detection presented in Fig. 32c, the fact that only one structure is captured is most likely related to the multiplicity of steps involved in this eduction scheme and the additional constraints invoked. It is interesting to note that the second step of this method corresponds to a pattern-recognition method and is similar to that used to generate the results presented in Fig. 32b. For these results, a correlation threshold of 0.9 was used while the Houston vorticity-based approach is *less critical* with only 0.8. Hence we must conclude that the combination of several different selection criteria (vorticity vs velocity for detection, constraints on spatial scale, etc.) leads to a more severe filter, and as a result, fewer structures are detected. This also indicates that eduction schemes based on multiple-sensor data are in general more reliable.

Note how the test of the pairing processes (positions noted in Fig. 32) is in good agreement with the visual analysis of the PFV (Fig. 4) and the sectional streamline (Fig. 23). As

discussed above, the structure detection frequency is typically the same (within a reasonable band) for the velocity-based schemes and is comparable to spectra results. The vorticity-based schemes, on the other hand, differ a great deal. The Houston scheme, for example, detects substantially fewer structures (about  $\frac{1}{4}$ – $\frac{1}{3}$  of the above average) while the Newcastle scheme detects substantially more (between two and three times the number of structure detection obtained from the velocity-based schemes). Typical numbers are presented below in the Ensemble Average section.

### 9.1.2 Instantaneous information from correlation-based techniques

Some salient common features between the conditional sampling results and the POD can be identified by examining the first POD mode representation of the sample time series as shown in Fig. 12b. Note that the second structure from the left is clearly identifiable by the first mode of the POD. Recall that this particular structure was at least partially detected by all the conditional methods and was the only one detected by the vorticity-based scheme. Therefore, it can be argued that detection methods based on the maximum of local vorticity agree with the structure of largest spatial extent detected by the first POD mode. This suggests that the dominant  $\omega_z$  structures are buried in the two-point statistics and, hence, in the POD eigenfunctions as well.

### 9.2 Ensemble average

It is important to obtain *ensemble averages* from the different identification techniques because of their potential application in closure schemes and physical interpretation. Some very useful quantitative comparisons can be made between the various techniques from this point of view. Such examples are the size of the ensemble averaged structure, denoted  $A_1$ , and the distance between braids (or between saddle points), denote  $A_2$ . Both of these can be estimated from the various figures.

The number of detected events used to build the ensemble averages are different, depending on the method employed. For the common study presented here, the order of magnitude of the detected events corresponding to 1 s of signal were typically: 400 for the WAG method (“v” detections), 900 for the Newcastle Vorticity-based scheme, 100 for the Houston Vorticity-based detection scheme, 300 for the Delocalized Conditional Sampling method and 240 for the Correlation technique. (Of course, these numbers depend to some degree on the threshold levels).

Table 3 summarizes the estimates of these two parameters for the various applications. References are made to the appropriate figures from which these values are extracted.

Note that the above values agree to within roughly  $\pm 6\%$ . This is quite remarkable considering the major differences between the techniques. Also note that the mean size of the ensemble averaged structure lies between  $2.8$  and  $3.2\delta_w$ . This corresponds well to established results for this type of flow, which typically exhibits an equivalent Strouhal number of  $0.33$ . It is interesting to note that for the schemes which permit the extraction of both  $A_1$  &  $A_2$  that these length scales are more

Table 3

Method	Figure	$A_1$ (mm)	$A_2$ (mm)
POD 1st mode	17b	94	–
Vorticity	22b, 22c	–	85
WAG	26	84	80
DCS	28a	90	91

or less the same. This indicates that the distance between structures and their length scales are similar and suggests that the individual structures should interact and influence one other.

### 9.3 Conclusion

This common study has shown that direct comparisons between results of several methods are now possible. Good quantitative and qualitative agreement between the different methods have been observed as well as some differences noted. For the first time, both instantaneous and ensemble averaged results were discussed utilizing the same sample. Some new opportunities for improving the techniques have been identified which involve taking advantage of the strengths of each method through combined applications. A particular example that comes to mind would be to apply the POD to obtain a global time-dependent coefficient to which wavelet analysis can be applied. Note that this may eliminate the sensitivity to spatial dependence and allow the conditional efficiency of the wavelet method to apply.

Several issues remain to be resolved. In particular, it is clear that the 3D character of CS should be taken into consideration. Experiments to obtain 3D information are complex and care must be taken to select the optimal experimental arrangements involving Hot Wire rakes, for example. The use of complementary techniques can also help to increase the possibilities of experimental studies. This is particularly important in view of the need for experiments which characterize the 3D structure by utilizing one or more education techniques.

### References

- Adrian RJ (1975) On the role of conditional averages in turbulence theory. In Proc 4th Biennial Symp on Turbulence in Liquids
- Adrian RJ; Moin P (1988) Stochastic estimation of organized turbulent structure: Homogeneous shear flow. J Fluid Mech 190: 531–559
- Antonia RA (1981) Conditional sampling in turbulence measurement Annual Rev Fluid Mech 13: 131–156
- Antonia RA; Bisset DK; Browne LWB (1990) Effect of Reynolds number on the organized motion in a turbulent boundary layer. In (Kline SJ, Afgan NH editors) Near Wall Turbulence, New York, Hemisphere, pp 488–506
- Antonia RA; Browne LWB; Bisset DK; Fulachier L (1987) A description of the organized motion in the turbulent far-wake of a cylinder at low Reynolds number. J Fluid Mech 184: 423–444
- Aubry N; Holmes P; Lumley J; Stone E (1988) Dynamics of coherent structures in the wall region of a turbulent boundary layer. J Fluid Mech 192, pp. 115–173
- Bacry E; Arneodo A; Frisch U; Gagne Y; Hopfinger E (1990) Wavelet analysis of fully developed turbulence data and measurement of scaling exponents. In: Turbulence and coherent structures (In: Métais O, Lesieur M, editors) Dordrecht, Kluwer, pp 203–215

- Bell JH; Mehta RD** (1992) Measurements of streamwise vortical structures in a plane mixing layer. *J Fluid Mech* 239: 213–248
- Bellin S** (1991) Etude expérimentale des structures cohérentes d'une couche de mélange plane turbulente de fluide incompressible. Thèse de l'Université de Poitiers
- Bellin S; Delville J; Vincendeau E; Garem JH; Bonnet JP** (1993) Large scale structure characterization in a 2D mixing layer by Pseudo-Flow-Visualization and Delocalized Conditional Sampling. In *Eddy structure identification in free turbulent shear flows*, Proceedings of the IUTAM Symp Poitiers October 1992 (Bonnet JP, Glauser MN, editors), Kluwer Academic Publishers: 91–102
- Berkooz G; Holmes P; Lumley JL** (1993) The proper orthogonal decomposition in the analysis of turbulent flows. *Ann Rev Fluid Mech* 25: 539–575
- Bernal LP** (1988) The statistics of the organized vortical structure in turbulent mixing layer. *Phys. Fluids* 31(9): 2533–2543
- Bernal LP; Roshko A** (1986) Streamwise vortex structure in plane mixing layers. *J Fluid Mech* 170: 499–525
- Bisset DK; Antonia RA; Browne LWB** (1990) Spatial organization of large structures in the turbulent far-wake of a cylinder. *J Fluid Mech* 218: 438–461
- Blackwelder RF; Kaplan RE** (1976) On the wall structure of the turbulent boundary layer. *J Fluid Mech* 76: 89–112
- Bonnet JP; Cole DR; Delville J; Glauser MN; Ukeiley LS** (1994) Stochastic estimation and proper orthogonal decomposition: complementary techniques for identifying structure. *Exp Fluids* 17: 307–314
- Bonnet JP; Delville J; Glauser MN** (1993) Workshop on eddy structure identification in free turbulent shear flows. *ERCFTAC Bull* 17: 41–51
- Bonnet JP; Lewalle J; Glauser MN** (1996) Coherent Structures: Past present and future. In *Advances in turbulence VI*. (Gravilakis S; Machiels L; Monkewitz PA, editors) Kluwer, Dordrecht, pp 83–90
- Breidenthal R** (1980) Response of plane shear layers and wakes to strong three-dimensional disturbances. *Phys Fluids* 23: 1929
- Brown GL; Roshko A** (1974) On density effects and large structure in turbulent mixing layers. *J Fluid Mech* 64: 775–816
- Browand FK** (1986) The structure of the turbulent mixing layer. *Physica D* 18: 135–148
- Browand FK; Ho CM** (1983) The mixing layer: an example of quasi two dimensional turbulence. *J Mécanique Théorique et Appliquée*, numéro spécial, pp 99–120
- Browand FK; Troutt TR** (1980) A note on spanwise structure in the two-dimensional mixing layer. *J Fluid Mech* 917: 771–781
- Browand FK; Troutt TR** (1985) The turbulent mixing layer; geometry of large vortices. *J Fluid Mech* 158: 489–509
- Browand FK; Weidman PD** (1976) Large scales in the developing mixing layer. *J Fluid Mech* 76: 127–144
- Bruun HH** (1995) *Hot-wire Anemometry – principles and signal analysis*, Oxford University Press, Oxford
- Cole DR; Glauser MN; Guezennec YG** (1992) An application of stochastic estimation to the jet mixing layer. *Phys Fluids A* 4: 192–194
- Courant R; Hilbert D** (1953) *Methods of mathematical physics. Vol. 1* Interscience, New York
- Dahlman U** (1990) On the footprints of three-dimensional separated vortex flows around blunt bodies. Attempts of defining and analysing complex flow structures. *Vortex Flow Aerodynamics. AGARD conference proceedings* 494: 9–1, 9–13, Neuilly
- Delville J** (1993) Characterization of the organization in shear layers via proper orthogonal decomposition. In *Eddy structure identification in free turbulent shear flows*. Proc IUTAM Symp – Poitiers October 1992 (Bonnet JP; Glauser MN, editors) Kluwer Academic Publishers, Dordrecht, pp 225–238
- Delville J** (1995) La décomposition orthogonale aux valeurs propres et l'analyse de l'organisation tridimensionnelle des écoulements turbulents cisailés libres. Thèse de l'Université de Poitiers, Janvier 1995
- Delville J; Bellin S; Bonnet JP** (1989) Analysis of structures in a turbulent, plane mixing layer by use of pseudo visualisation method based on hot-wire anemometry. In: *Advances in turbulence*, 2 (Fernholz HH; Fiedler HE, editors) Springer, Berlin, pp 251–256
- Delville J; Chahine Z; Bonnet JP** (1987) Experimental study of an incompressible, plane mixing layer by temporal and spectral analysis. In: *Advances in turbulence 1* (Comte-Bellot G; Mathieu J, editors) Springer, Berlin, pp 435–444
- Delville J; Vincendeau E; Ukeiley L; Garem JH; Bonnet JP** (1993) Etude expérimentale de la structure d'une couche de mélange plane turbulente en fluide incompressible. Application de la décomposition orthogonale aux valeurs propres. Convention DRET 90-171 Rapport Final
- Farge M** (1992) Wavelet transforms and their applications to turbulence. *Ann Rev Fluid Mech* 24: 395–457
- Ferré JA; Giralt F** (1993) A pattern recognition approach to the analysis of turbulent signals. In: *Eddy structure identification in free turbulent shear flows*. Proc of the IUTAM Symp – Poitiers October 1992 (Bonnet JP; Glauser MN, editors) Kluwer Academic Publishers, Dordrecht, pp 181–194
- Glauser MN; George WK** (1987) An orthogonal decomposition of the axisymmetric jet mixing layer utilizing cross-wire velocity measurement. Proc 6th Symp Turbulent Shear Flows, Toulouse
- Glauser MN; George WK** (1992) Application of multipoint measurements for flow characterization. *Exp Thermal Fluid Sci* 5: 617–632
- Glauser MN; Cole D; Ukeiley LS; Bonnet JP; Delville J** (1993) Stochastic estimation and proper orthogonal decomposition: complementary technique for identifying structure. Proc Turbulent Shear Flow 9 Kyoto August 1993
- Grossman A; Morlet J** (1984) Decomposition of Hardy functions into square integrable wavelets of constant shape. *SIAM J Math Anal* 15: 723–736
- Guezennec YG** (1989) Stochastic estimation of coherent structures in turbulent boundary layers. *Phys Fluids A* 1: 1054–1060
- Ha Minh Hieu** (1994) Order and disorder in turbulent flows: their impact on turbulence modelling. Osborne Reynolds Centenary Symposium, UMIST Manchester
- Higuchi H; Lewalle J; Crane P** (1994) On the structure of two-dimensional wakes behind a pair of flat plates. *Phys Fluids A* 6, 297–305
- Ho CM; Huerre P** (1984) Perturbed Free Shear Layers. *Annual Review of Fluid Mechanics*. 16: 365
- Hunt JCR; Abell CJ; Peterka JA; Woo H** (1978) Kinematic studies of the flow around free or surface-mounted obstacles; applying topology to flow visualization. *J Fluid Mech* 86: 179–200
- Hunt JCR; Carruthers DJ** (1990) Rapid distortion theory and the 'problems' of turbulence. *J Fluid Mech* 212: 497–532
- Hunt JCR; Vassilicos JC** (1991) Kolmogorov's contributions to the physical and geometrical understanding of small-scale turbulence and recent developments. *Proc R Soc Lond A* 434: 183–210
- Hussain F** (1983) Coherent structures-reality and myth. *Physics of Fluids* 26: 2816–2850
- Hussain F** (1993) Understanding coherent structures through vortex dynamics. In: *Eddy structure identification in free turbulent shear flows*. Proc IUTAM Symp – Poitiers October 1992 (Bonnet JP; Glauser MN, editors) Kluwer Academic Publishers, Dordrecht, pp 13–26
- Hussain F; Hayakawa M** (1987) Eduction of large-scale organized structure in a plane turbulent wake. *J Fluid Mech* 180: 193–229
- Jeong J; Grinstein FF; Hussain F; Albanis N** (1993) Eduction of coherent structures in a numerically simulated plane wake. In: *Eddy structure identification in free turbulent shear flows*. Proc IUTAM Symp – Poitiers October 1992 (Bonnet JP; Glauser MN, editors) Kluwer Academic Publishers, Dordrecht, pp 65–76
- Jiménez J; Wray AA; Saffman PG; Rogallo RS** (1993) The structure of intense vorticity in isotropic turbulence. *J Fluid Mech* 255: 65–90

- Kaplan W** (1958) Ordinary differential equations. Addison-Wesley, Reading
- Kevlahan NKR; Hunt JRC; Vassilicos JC** (1993) A comparison of different analytical techniques for identifying structures in turbulence. In: Eddy structure identification in free turbulent shear flows. Proc IUTAM Symp – Poitiers October 1992 (Bonnet JP; Glauser MN, editors) Kluwer Academic Publishers, Dordrecht, pp 311–324
- Konrad JH** (1976) An experimental investigation of mixing in two-dimensional turbulent shear flows with applications to diffusion-limited chemical reaction. Ph.D. Thesis, California Institute of Technology
- Lasheras JC; Cho JS; Maxworthy T** (1986) On the origin and evolution of stream-wise vortical structures in a plane, free shear layer. *J Fluid Mech* 172: 231–258
- Lasheras JC; Choi H** (1988) Three-dimensional instability of a plane free shear layer: an experimental study of the formation and evolution of streamwise vortices. *J Fluid Mech* 189: 53–86
- Lasheras JC; Meiburg E** (1990) Three-dimensional vorticity modes in the wake of a flat plate. *Phys Fluids* 2: 371
- Lesieur M** (1993) Understanding coherent vortices through computational fluid dynamics. *Theoretical and Comput. Fluid Dyn.* 5: 177–193
- Lewalle J** (1994) Wavelet analysis of experimental data: some methods and the underlying physics. AIAA paper 94-2281
- Liepmann HW; Laufer J** (1947) Investigations of free turbulent mixing. N.A.C.A. Technical Note No. 1257
- Liu JTC** (1989) Coherent structures in transitional and turbulent free shear flows. *Ann Rev Fluid Mech* 21: 285–315
- Lumley JL** (1967) The structure of inhomogeneous turbulent flows. In atmospheric turbulence and Radio wave propagations. (Yaglom AM; Tatarsky VI, editors) Nauka, Moscow pp 166
- Maekawa H; Nozaki T; Ohasako S** (1988) Coherent structures in the turbulent plane for wake behind a split plate. 11th Symp on Turbulence Missouri-Rolla October 1988
- Mallat S** (1989) A theory for multiresolution signal decomposition: the wavelet representation. *IEEE Trans. Pattern Anal Mechine Intell* 31: 674–693
- Meiburg E; Lasheras JC** (1988) Experimental and numerical investigation of the three-dimensional transition in plane wakes. *J Fluid Mech* 190: 1–37
- Meneveau C** (1991) Analysis of turbulence in the orthonormal wavelet representation. *J Fluid Mech* 232: 469–520
- Metcalfe RW; Hussain F; Menon S; Hayakawa M** (1987) Turbulent shear flows 5, (Durst F et al. editors) Springer, Berlin, pp 110–123
- Moser RD; Rogers MM** (1993) Coherent structures in a simulated turbulent mixing layer. In: Eddy structure identification in free turbulent shear flows. Proc of the IUTAM Symp — Poitiers October 1992 (Bonnet JP; Glauser MN, editors), Kluwer Academic Publishers, Dordrecht, pp 415–428
- Mumford JC** (1982) The structure of the large eddies in fully developed turbulent shear flow. Part 1. The plane jet. *J Fluid Mech* 118, 241
- Perry AE; Chong MS** (1986) A series expansion study of the Navier–Stokes equations with application three-dimensional separation patterns. *J Fluid Mech* 173: 207–223
- Pierrehumbert RT; Widnall SE** (1982) The two- and three-dimensional instabilities of a spatially periodic shear layer. *J Fluid Mech* 114: 59
- Reynolds WC; Hussain F** (1972) The mechanisms of an organized wave in turbulent shear flow. Part 3. Theoretical models and comparisons with experiments. *J Fluid Mech* 54 part 2: 263–288
- Tennekes H; Lumley J** (1972) A first course in turbulence. MIT Press, Cambridge
- Townsend AA** (1979) Flow patterns of large eddies in a wake and in a boundary layer. *J Fluid Mech* 95 Part 3: 515–537
- Tso J; Hussain F** (1989) Organized motions in a fully developed turbulent axisymmetric jet. *J Fluid Mech* 203: 425–448
- Tung TC; Adrian RJ** (1980) Higher-order estimates of conditional eddies in isotropic turbulence. *Phys Fluids* 23: 1469–1470
- Ukeiley LS** (1995) Dynamics of large scale structures in a plane turbulent mixing layer. MAE report, Clarkson University, USA
- Ukeiley LS; Cole DR; Glauser MN** (1993) An examination of the axisymmetric jet mixing layer using coherent structure detection techniques. In: Eddy structure identification in free turbulent shear flows. Proc of the IUTAM Symp — Poitiers October 1992 (Bonnet JP; Glauser MN, editors), Kluwer Academic Publishers, Dordrecht, pp 325–336
- Vassilicos JC; Hunt JCR** (1991) Fractal dimensions and spectra of interfaces with application to turbulence. *Proc R Soc Lond A* 435: 550–534
- Winant CD; Browand FK** (1974) Vortex pairing: the mechanism of turbulent mixing-layer growth at Moderate Reynolds Number. *J Fluid Mech* 63: 237–255
- Zaman KMBQ; Hussain AKMF** (1984) Natural large-scale structures in the axisymmetric mixing layer. *J Fluid Mech* 138: 325–351

#### Proceedings of recent meetings devoted to Structure Identification and Analysis

- [Dubrovnik 1988] Zoran P. Zaric Memorial International Seminar on Near-Wall Turbulence Dubrovnik, May 1988
- [Cambridge 1989] Topological fluids dynamics IUTAM Symposium Cambridge 1989. Moffatt HK; Tsinober A editors
- [Grenoble 1990] Turbulence and coherent structures, selected papers from Turbulence 89: Organized structures and turbulence in fluid mechanics, Grenoble Sept. 1989 Métais O; Lesieur M, editors, Kluwer Academic Publisher, 1990
- [Ithaca 1990] Wither turbulence? Turbulence at the crossroads, Proc, Ithaca, NY, 1989, Lumley J, editor, Springer, Berlin, 1990
- [Langley 1990] Boundary layer structure Workshop, Langley Res. Center, Hampton, VA, Aug. 1990
- [Zürich 1990] Structure of turbulence and drag reduction, IUTAM Symp. Zurich 1989, Gyr A, editor, Springer, Berlin, 1990
- [Tucson 1990] Turbulence theories and models incorporating experimental and computer simulation knowledge of coherent structures, Wallace JM, Symp ASME, Appl Mech Rev 43, 5, 2, S201, 1990
- [Langley 1992] Studies in turbulence, Gatski TB; Sarkar S; Speziale CG, editor Springer, Berlin, 1992
- [Poitiers 1992] Eddy structure identification in free turbulent shear flows. Proc. IUTAM Symp – Poitiers October 1992 (Bonnet JP; Glauser MN, editors) Kluwer Academic Publishers, Dordrecht, 1993
- [Udine 1994] Eddy structure identification. Contributors: Adrian R; Bonnet JP; Delville J; Hussain F; Lumley J; Métais O; Vassilicos C (1996) CISM courses and lectures No. 353, Bonnet JP, Editor, Springer, Berlin, 1996.